COMPARISON OF SUPERCRITICAL CO2 WITH WATER AS GEOFLUID IN GEOTHERMAL RESERVOIRS WITH NUMERICAL INVESTIGATION USING FULLY COUPLED THERMO-HYDRO-GEOMECHANICAL MODEL

Journal of Energy Resources Technology. Received December 23, 2021;
Accepted manuscript posted August 28, 2022. doi:10.1115/1.4055538

COMPARISON OF SUPERCRITICAL CO_2 WITH WATER AS GEOFLUID IN GEOTHERMAL RESERVOIRS WITH NUMERICAL INVESTIGATION USING FULLY COUPLED THERMO-HYDRO-GEOMECHANICAL MODEL

Manojkumar Gudala, first author
Ali I. Al-Naimi Petroleum Engineering Research Center, Physical Science and Engineering Division, King Abdullah University of Science and Technology (KAUST), Thuwal, 23955-6900, Saudi Arabia
Energy Resources and Petroleum Engineering Program, Physical Science and Engineering Division, King Abdullah University of Science and Technology (KAUST), Thuwal, 23955-6900, Saudi Arabia
e-mail: manojkumar.gudala@kaust.edu.sa

Suresh Kumar Govindarajan, second author[1]
Professor,
Reservoir Simulation Laboratory,
Petroleum Engineering Programme,
Department of Ocean Engineering,
Indian Institute of Technology, Madras, India-600036e-mail
e-mail: gskumar@iitm.ac.in

Bicheng Yan, Third author[2]
Ali I. Al-Naimi Petroleum Engineering Research Center, Physical Science and Engineering Division, King Abdullah University of Science and Technology (KAUST), Thuwal, 23955-6900, Saudi Arabia
Energy Resources and Petroleum Engineering Program, Physical Science and Engineering Division, King Abdullah University of Science and Technology (KAUST), Thuwal, 23955-6900, Saudi Arabia
e-mail: bicheng.yan@kaust.edu.sa

[1] Suresh kumar Govindarajan: gskumar@kaust.edu.sa
[2] Bicheng Yan: bicheng.yan@kaust.edu.sa
[3] Shuyu Sun: shuyu.sun@kaust.edu.sa

Shuyu Sun, Fourth author[3]
Computational Transport Phenomena Laboratory (CTPL), Physical Science and Engineering Division (PSE), King Abdullah University of Science and Technology (KAUST), Thuwal, 23955-6900, Saudi Arabia
Energy Resources and Petroleum Engineering Program, Physical Science and Engineering Division, King Abdullah University of Science and Technology (KAUST), Thuwal, 23955-6900, Saudi Arabia
Earth Science and Engineering Program, Physical Science and Engineering Division, King Abdullah University of Science and Technology (KAUST), Thuwal, 23955-6900, Saudi Arabia.
e-mail: shuyu.sun@kaust.edu.sa

ABSTRACT

In the present work, fully coupled dynamic thermo-hydro-mechanical (THM) model was employed to investigate the advantage and disadvantages of supercritical CO_2 ($SCCO_2$) over water as geofluids. Low-temperature zone was found in both $SCCO_2$-EGS and water-EGS systems, but spatial expansion is higher in water-EGS. Although, the spatial expansion of $SCCO_2$ into the rock matrix will help in the geo-sequestration. The expansion of stress and strain invaded zones were identified significantly in the vicinity of fracture and injection well. $SCCO_2$-EGS system is giving better thermal breakthrough and geothermal life conditions compared to the water-EGS system. Reservoir flow impedance (RFI) and heat power are examined, and heat power are high in the water-EGS system. Minimum RFI is found in the $SCCO_2$-EGS system at $45°C$ and 0.05 m/s. Maximum heat power for $SCCO_2$-EGS was observed at $35°C$, 20 MPa, and 0.15 m/s. Therefore, the developed dynamic THM model is having greater abilities to examine behaviour of $SCCO_2$-EGS and water-EGS systems effectively. The variations occur in the rock matrix and the performance indicators are dependent on the type of fluid, injection/production velocities, initial reservoir pressure, injection temperature. The advantages of $SCCO_2$-EGS system over the water-EGS system, providing a promising result to the geothermal industry as geofluid.

Keywords: *$SCCO_2$-EGS, water-EGS, geofluid, thermo-hydro-geomechanical, reservoir flow impedance, heat power*

Journal of Energy Resources Technology. Received December 23, 2021;
Accepted manuscript posted August 28, 2022. doi:10.1115/1.4055538

1. Introduction

Energy demand and carbon emissions from the fossil fuels have become critical issues in the many developed and developing countries. To meet the energy requirement geothermal is the prominent resource due to its availability and it is clean, ecofriendly, and the renewable resource [1–5]. The amount of geothermal energy resource is estimated as 40-400 M EJ (1EJ=10^{18}J) and it is approximately 100-1000 folds than fossil fuels [6]. Enhanced geothermal systems will be producing heat from the low porosity and low permeable zones to meet the energy requirements. The carbon dioxide emissions from the fossil fuels will lead to increase global warming. Capturing and geological storing of CO_2 have been major options for sequestering CO_2; the deep oil/gas reservoirs, and deep saline aquifers are used for geological storing purpose.

In the recent years, the CO_2 becoming most attractive as an alternative geo fluid for extracting heat from the geothermal reservoirs. Brown first proposed the advantages of CO_2 as geofluid compared to the water [7]. High compressibility, expansivity, and low viscosity are the advantages of CO_2 over the water. These will increase the mobility in the rock matrix and fracture compared to water. This will also reduce the pumping power required to inject the geofluid into the hot rock to extract the heat. Another advantage of the fluid from the prospect of the geo sequestration, if the fluid loss occurs from the main hydraulic fractures in to rock matrix can have ability to permanently sequester the CO_2 [8–14]. In the geothermal reservoirs, hydraulic fractures play an important role in the heat extraction. This is because of the higher fracture permeability compared to the rock matrix [13,15–18]. The thermal energy recovered from the geothermal reservoir by injecting the relatively low temperature fluid into the hydraulic fracture from injection well and producing high temperature fluid at the production well (i.e., the heat collecting from the rock matrix) [17,19–22]. Fractures act as preferential flow channels in the geothermal reservoir for carrying cold fluid from injection location to production location and extracting heat energy from the rock matrix [10,23–26]. Geothermal reservoir performance during the thermal energy production is mainly rely on the magnitude permeable channels/fractures in the rock matrix for the movement of geofluid [27–29]. Development of geofluid flow field in the porous/fracture media is highly reliant on the

Journal of Energy Resources Technology. Received December 23, 2021;
Accepted manuscript posted August 28, 2022. doi:10.1115/1.4055538

thermal discrepancy in the rock matrix [27–32], which will be altering the temperature of surrounding rock matrix. It can generate the variations in the porous media will lead to compaction and expansion. Therefore, the type of fluid and physical properties and the fracture and rock properties will play a key role in the heat production of geothermal reservoir.

The advantages of super critical CO_2 (SCCO_2) over the water as geofluid in the geothermal reservoir for heat extraction is gaining more importance. Several researchers found that the SCCO_2 showing promising numerical results due to the high compressibility, high expansivity, low viscosity, low density, and low chemical interaction with the rock matrix over the water [8–14,33–38]. Pan et al. [34] studied the injection of supercritical CO_2 into a permeable reservoir which is initially saturated with warer using coupled wellbore-reservoir system. They also conducted the sensitivity analysis on the mass flow rate, injection temperatre, and reservoir permeability. They found theat these parameters influencing the extraction of heat from the reaervoir. Biagi et al [8] proposed an injection scenarios used the TOUGH2 for the simulating the geothermal reservoir for heat production using SCCO_2. They mentioned that the decline in the heat extraction rate due to the cooling of the reservoir. Liang et al [33] investigated the interactions of water/+gas(CO_2) in the geothermal reaservoir for the production of heat. They inclueded the variation of porosity and permeability as functions of geochemical reactions initiated by the injection of CO_2 into hot reservoir. They didn't consider the variation of other properties of rock and fluid properties while injection/extraction heat. Yin et al [36] is also workind on the injection of CO_2 into the porous media with cahnge in porosity and permeability in a carbonate reservoir. Zhang et al [37] investigated the impact of CO_2-EGS and water-EGS interms of net power, thermal efficiency, and exergy efficiency. They found that CO_2-EGS porodeuces more power comparedd to the water-EGS system. Zhang et al [11] workind on the CO_2 assisted heat recovery from the high temperature gas well using the CMG-star simulator. Most the researchers are not considered the dynaic behaviour of the reservoir and the fluid in their research.

From the abovementioned, the present work is focused on the comparison of super critical CO_2 ($SCCO_2$) as geofluid with water using the dynamic behaviour of rock matrix, fracture and also the fluid properties. The evolution of rock properties, fluid properties, and temperature with $SCCO_2$ were examined exclusively with the comparison of water. The properties of the injection fluids are considered above the super critical condition for both CO_2 and water. In additions to that the performance parameters/indicators such as reservoir impedance, geothermal life, breakthrough time, and heat power are determined for the evaluation and development purpose. The influence of injection/production velocities, initial reservoir pressure and also the injection temperature on the production temperature, reservoir flow impedance, and heat power are examined for both $SCCO_2$ and water and also comparison between them also presented.

2. Mathematical Equations

2.1 Governing equations

The mathematical equation which will govern the transfer of heat in the rock matrix is presented in Eq. (1).

$$\left(\rho C_p\right)_{eff}\frac{\partial T}{\partial t}+\rho_{fl}C_{pfl}u_{mat}.\nabla T-\nabla\cdot(\lambda_{eff}\nabla T)=Q_{mT}+Q_{fT} \quad \text{...... (1)}$$

$$\left(\rho C_p\right)_{eff}=\phi_{mat}\rho_{fl}C_{pr}+\left(1-\phi_{mat}\right)\rho_{mat}C_{pfl} \quad \text{...... (2)}$$

$$\lambda_{eff}=\phi_{mat}\lambda_{mat}+\left(1-\phi_{mat}\right)\lambda_{fl} \quad \text{...... (3)}$$

$$u_{mat}=-\frac{\kappa_{mat}}{\mu_{fl}}\nabla p_{mat} \quad \text{...... (4)}$$

The mathematical equation which will govern the transfer of heat in the fracture is given in Eq. (5)

$$a_{frc}\left[\left(\rho C_p\right)_{eff}\right]_{frc}\frac{\partial T}{\partial t}+a_{frc}\left(\rho_{fl}C_{pw}\right)_{frc}u_{frc}.\nabla T-\nabla\cdot a_{frc}(\lambda_{eff})_{frc}\nabla T=a_{frc}\left(Q_{fT}+Q_{mT}\right) \quad \text{...... (5)}$$

The fluid flow velocity in fracture (u_{frc}) is given in Eq. (6)

$$u_{frc}=-\frac{\kappa_{frc}}{\mu_{fl}}\nabla p_{frc}=\frac{-a_{frc}{}^{2}}{12\mu_{fl}}\nabla p_{frc} \quad \text{...... (6)}$$

Journal of Energy Resources Technology. Received December 23, 2021;
Accepted manuscript posted August 28, 2022. doi:10.1115/1.4055538

The injected cold fluid flow in the porous media and fracture are administrated by the Darcy's law, mass conservation law, compressibility equation and the force equilibrium equations in the porous media.

The mathematical equation which will govern the geofluid flow in the rock matrix is given in Eq. (7) [39].

$$\frac{\partial\left(\phi_{mat}\rho_{fl}\right)}{\partial t}-\nabla\cdot\left[\rho_{fl}\frac{\kappa_{mat}}{\mu_{fl}}\nabla p_{mat}\right]-q_{mat}=0 \qquad \text{...... (7)}$$

The mathematical equation for the poroelastic storage model is given in Eq. (8).

$$\frac{\partial\left(\rho_{fl}\phi_{mat}\right)}{\partial t}=\frac{\rho_{fl}}{M}\frac{\partial p_{mat}}{\partial t} \qquad \text{...... (8)}$$

The Biot's modulus and Biot-Willis coefficient (α_b) are given in Eq. (9) and Eq. (10)[40,41].

$$\frac{1}{M}=\frac{\phi_{mat}}{K_{fl}}+\left(\alpha_b-\phi_{mat}\right)\frac{1-\phi_{mat}}{K_d} \qquad \text{...... (9)}$$

$$\alpha_b=1-\frac{K_d}{K_{fl}} \qquad \text{...... (10)}$$

The mathematical equation which will govern both the geofluid flow and geomechanical effects in the porous media is presented in Eq. (10) (i.e., after merging Eq. (7) to Eq. (10)).

$$\left(\frac{\phi_{mat}}{K_{fl}}+\left(1-\frac{K_d}{K_{fl}}-\phi_{mat}\right)\frac{1-\phi_{mat}}{K_d}\right)\frac{\partial p_{mat}}{\partial t}-\nabla\cdot\left(\frac{\kappa_{mat}}{\mu_{fl}}\nabla p_{mat}\right)+\left(1-\frac{K_d}{K_{fl}}\right)\frac{\partial\varepsilon_{vol}}{\partial t}=0 \qquad \text{...... (11)}$$

The volumetric strain (ε_{vol}) is given in the form of displacement vectors and presented in Eq. (12).

$$\varepsilon_v=\varepsilon_{11}+\varepsilon_{22} \qquad :\left(\varepsilon_{ij}=0.5\left(\partial u_{di}/\partial x_j+\partial u_{dj}/\partial x_i\right)\right) \qquad \text{...... (12)}$$

The mathematical equation for the flow of geofluid in the fracture is given in Eq. (13)

$$a_{frc}\frac{\partial}{\partial t}\left(\phi_{frc}\rho_{fl}\right)+\nabla_{Tn}\cdot\left(\rho_{fl}q_{frc}\right)=a_{frc}q_{mat} \qquad \text{...... (13)}$$

The mathematical equation for the flow rate of geofluid (q_{frc}) per unit length in the fracture is presented in Eq. (14)

$$q_{frc} = -\frac{\kappa_{frc}}{\mu_{fl}} a_{frc} \nabla_{Tn} p_{frc} = \frac{-a_{frc}{}^{3}}{12\mu_{fl}} \nabla_{Tn} p_{frc} \quad \text{...... (14)}$$

The governing equation for the force balance for the poroelastic rock matrix is presented in Eq. (15) [3,21,42–44]

$$\nabla \cdot \sigma + \left(\rho_{fl}\phi_{mat} + \rho_{mat}\right) = 0 \quad \text{and} \quad \sigma = \sigma_{mat} - \alpha_b p_{mat} \quad \text{...... (15)}$$

The hydraulic fracture is taken as thin elastic layer. Force per unit area acting on the fracture is represented mathematically as a function of spring constant (k_A), damping constant per unit area (d_A) and fracture thickness (or fracture aperture) (a_{frc}) is given in the following eq. (16).

$$F_A = -k_A\left(u_u - u_d - u_0\right) - d_A \frac{\partial\left(u_u - u_d - u_0\right)}{\partial t} - \frac{1}{2}\rho_{fl} a_{frc} \frac{\partial^2\left(u_u + u_d\right)}{\partial t^2} \quad \text{...... (16)}$$

Spring constant for unit area is given in eq. (17)

$$k_A = k_n\, n \otimes n + k_s\left(I - n \otimes n\right) \quad \text{...... (17)}$$

The stiffness in the normal direction, and shear stiffness are defined as a function of both elastic modulus and Poisson's ratios of fractures are given in eq. (18) and eq. (19), respectively.

$$k_n = \frac{E_{frc}\left(1-\upsilon_{frc}\right)}{a_{frc}\left(1+\upsilon_{frc}\right)\left(1-2\upsilon_{frc}\right)} \quad \text{...... (18)}$$

$$k_s = \frac{E_{frc}}{2a_{frc}\left(1+\upsilon_{frc}\right)} \quad \text{...... (19)}$$

2.2 Coupling mathematical relations

Variation of porosity in rock matrix is defined as a changes occur geomechanical and thermal strains and is presented in Eq. (20) [43,45].

$$\phi_{mat} = \frac{\phi_i + \Delta\varepsilon_v - \Delta\varepsilon_T}{1+\Delta\varepsilon_v} = \frac{\phi_i + \Delta\varepsilon_v - \left[\alpha_T\left(1-\phi_i\right)\Delta T\right]}{1+\Delta\varepsilon_v} \quad \text{...... (20)}$$

The elastic modulus of reservoir is considered as a function of porosity variation and presented in Eq. (21) and it is developed by the Liu [46].

$$\ln\left(\frac{E}{E_i}\right) = -d\left(\phi_{mat} - \phi_i\right) \quad \text{...... (21)}$$

Journal of Energy Resources Technology. Received December 23, 2021;
Accepted manuscript posted August 28, 2022. doi:10.1115/1.4055538

The rock matrix and fracture permeabilities are given Eq. (22) and Eq. (23), respectively [47–49].

$$\ln\left(\frac{\kappa}{\kappa_o}\right)=\left[\frac{(1-\phi_i)a+b\phi_i}{\phi_i}\right]\varepsilon_v=C_n\varepsilon_v \qquad \text{...... (22)}$$

$$\kappa_{frcN}=\kappa_{frc0}\exp\left(-\frac{\sigma_n}{\sigma^*}\right) \qquad \text{...... (23)}$$

The rock heat capacity of rock, thermal conductivity of rock are presented in Eq. (24) and Eq.(25) [43,50] and

$$C_{pr}(\kappa)=\begin{cases}\dfrac{(2.6\log(\kappa)+4.2)\times10^3}{2.7\log(\kappa)+0.3}; & \text{if } -20\le\log(\kappa)\le-11\\ -13.0\log(\kappa)+699.0; & \text{if } -11\le\log(\kappa)\le-2\end{cases} \qquad \text{...... (24)}$$

$$\lambda_r(T)=2.6-0.0025(T-293.15) \qquad \text{...... (25)}$$

Temperature dependent viscosity, density, heat capacity and thermal conductivity were used in the present work. When water is used as geofluid Eq. (26) to Eq (29) [47,51] are utilized.

$$\mu_w(T)=\begin{cases}\begin{pmatrix}1.38-0.028T+1.36\times10^{-4}T^2\\ -4.61\times10^{-7}T^3+8.9\times10^{-10}T^4\\ -9.08\times10^{-13}T^5+3.84\times10^{-16}T^6\end{pmatrix}; & \text{if } 0\le T\le140\\ \begin{pmatrix}0.004-2.11\times10^{-5}T+3.86\times10^{-8}T^2\\ +2.4\times10^{-11}T^3\end{pmatrix}; & \text{if } 140\le T<280\end{cases} \qquad \text{...... (26)}$$

$$\rho_w(T)=838.47+1.40T-0.003T^2+3.72\times10^{-7}T^3 \qquad \text{...... (27)}$$

$$C_{pw}(T)=12010.15-80.41T+0.31T^2-5.38\times10^{-4}T^3+3.62\times10^{-7}T^4 \qquad \text{...... (28)}$$

$$\lambda_w(T)=-0.869+0.009T-1.58\times10^{-5}T^2+7.98\times10^{-9}T^3 \qquad \text{...... (29)}$$

The variation of thermophysical properties of super critical CO_2 such as viscosity, density, heat capacity and thermal conductivity are given in Eq. (30) to (33). These properties are dependent on the temperature and pressure. These equations will be applicable for a temperature range between 273 K to 553 K and pressure range between 15 MPa to 40 MPa [35].

Journal of Energy Resources Technology. Received December 23, 2021;
Accepted manuscript posted August 28, 2022. doi:10.1115/1.4055538

$$\mu_{\mathrm{scCO_2}}(T,p)=\begin{bmatrix}7.14\times10^{-9}T^2-5.642\times10^{-6}T-5.71\times10^{-9}p^2\\+2.186\times10^{-6}p+0.0011\end{bmatrix} \quad \text{...... (30)}$$

$$\rho_{\mathrm{scCO_2}}(T,p)=\begin{bmatrix}0.00036T^3-0.3693T^2+122T-0.333p^2\\+32.54p-12720\end{bmatrix} \quad \text{...... (31)}$$

$$C_{\mathrm{scCO_2}}(T,p)=\begin{bmatrix}-4.9\times10^{-5}T^3+0.084T^2-49.11T+0.47p^3\\-42.1p^2+1200p+276.3\end{bmatrix} \quad \text{...... (32)}$$

$$\lambda_{\mathrm{scCO_2}}(T,p)=\begin{bmatrix}-1.75\times10^{-8}T^3+2.29\times10^{-5}T^2-0.01T-1.89\times10^{-5}p^3\\+0.0007p^2-0.006p+1.46\end{bmatrix} \quad \text{...... (33)}$$

3. Model Implementation in COMSOL

3.1 Computational Model

In this work, we created a 2D computational domain with fracture of length 200 m as portrayed in Fig 1. Production and Injection wells are connected with the hydraulic fracture and is depicted in Fig 1a. it is considered as a main flow channel for the geofluid which is injected from the injection well and fluid is extracted at the production well. The computational porous domain is having an permeability of $9.87\times10^{-16}\ \mathrm{m}^2$ with initial porosity of 0.04. The size of the reservoir domain is considered as 500 m by 500 m and it is sufficient to prevent the consequences from the boundaries while extraction process. Quadrilateral meshing technique was employed in the present work with a size 0.1 m and having a total number of 25000000 domain elements and 210000 boundary elements in the meshed domain (Fig 1b). The properties of rock, fracture and geofluid (i.e., water/$SCCO_2$) are given in Table 1.

3.2 Initial and boundary conditions

The initial temperature of the geothermal reservoir is 425 K with and average reservoir pressure is 15 MPa. The computational porous domain is suitable to restrict the effects of boundaries during the heat recovery from the matrix while in operation. It will keep the constant temperatures at the boundaries which is equals to the initial reservoir temperature. The initial conditions of fluid flow, temperature and displacements field are given in eq. (34), eq. (35), eq. (36) and eq. (37), respectively.

$$p(x,y,t)\big|_{t=0}=p_0 \quad \text{...... (34)}$$

$$T\left(x,y,t\right)\Big|_{t=0}=T_0 \quad \text{...... (35)}$$

$$\left[u_x,u_y\right]^T\Big|_{t=0}=\left[0,0\right]^T \quad \text{...... (36)}$$

$$\left[\frac{\partial u_x}{\partial t},\frac{\partial u_y}{\partial t}\right]^T\Bigg|_{t=0}=\left[0,0\right]^T \quad \text{...... (37)}$$

For the fluid flow, undrained condition was employed on the all boundaries of the reservoir domain. In the structural module, as represented in the Fig 1b, two boundaries were constrained with rolling boundary condition and two boundaries are constrained by the lateral stresses. This study is attentive to the generation stress due to the thermal, pore pressure and external stress/loads effects during the heat production. The temperature of the geofluid (water or $SCCO_2$) was varied from 35 ℃ to 45 ℃ with variable injection rates between 0.05 m/s to 0.15 m/s. The initial fracture aperture is 0.5 mm with a fracture length of 200 m, and Biot-Willie's coefficient is 0.5 considered in the present work. Physical fields such as pressure, temperature, and displacement are examined in the present work during the heat extraction process by fully coupled model.

The boundary conditions are primarily concerned at injection well, production well and at the boundaries of the rock matrix. The fluid flow boundary conditions at the injection well and production well are represented in Eq. (38) and Eq. (39), respectively.

At injection well: $\dot{\mathrm{m}}\left(t\right)\big|_{\mathrm{inj}}=u_{inj}\rho_{fl}$ ...... (38)

At production well: $\dot{\mathrm{m}}\left(t\right)\big|_{prod}=u_{inj}\rho_{fl}$ ...... (39)

Heat flux boundary condition was employed at the injection well and is given in eq. (40).

At injection well: $q\big|_{\mathrm{inj}}=\left(C_p\right)_{fl}\left(T_{inj}-T_0\right)u_{inj}\rho_{fl}$ ...... (40)

3.3 Implementation in COMSOL Multiphysics

COMSOL Multiphysics 5.4 (Institute license version from the IIT-Madras) was used in the present research work. Plentiful researchers and engineers utilized the COMSOL Multiphysics for the fully coupled numerical investigations [25,44,52–57]. COMSOL inbuilt modules are used in the present work to investigate the coupled impact of THM interactions both in the fracture and rock matrix. The modules used in the present work

Journal of Energy Resources Technology. Received December 23, 2021;
Accepted manuscript posted August 28, 2022. doi:10.1115/1.4055538

are heat transfer in porous media, Darcy law, and solid mechanics along with the poroelasticity and thermal expansion modules. In addition to those modules, dynamics fluid and rock/fracture properties were embedded as local variable in the component section. The comparison of the fluid properties of water and $SCCO_2$ is depicted in the Fig 2. It was found that $SCCO_2$ has much less values in all the properties compared to the water in the operating conditions. In the geomechanics module (i.e., solid), hydraulic fracture is designated as a thin elastic layer's boundary element. The governing equations for the elastic layers are presented from Eq. 16 to Eq. 19. The fluid and heat flow in the fracture is employed using the fracture flow submodule was employed. The flow chart for solving the proposed THM model is presented in Fig 3. To stabilize the model, initially a stationary solver without boundary conditions was employed (i.e., with initial conditions) and then time dependent solver for 30 years.

4. Results and Discussion

4.1 Verification

Porous media with fracture will create complexity in dealing which will increase the intricacy in computational solving. To solve the developed fully coupled dynamic mathematical model we used the COMSOL Multiphysics, and it is a finite element tool. In the present work, hydraulic fracture is considered as the main conduit flow channel. Dynamic fluid and rock/fracture properties were explicitly employed using Eq. (20) to Eq. (33). The developed dynamic THM model and its accuracy are validated with the work of Lauwerie's [58]. Fig 4a represents the geometry with single fracture for the verification of transfer of heat. The equation for the spatiotemporal (i.e., *x*, and *t*) variation of temperature is given in Eq. (41)[58].

$$T\left(x,t\right)=T_0+\left(T_{inj}-T_0\right)erfc\left[\frac{\left(\lambda_m x/\rho_{fl}C_{pfl}a_{frc}\right)}{\sqrt{\frac{\lambda_m}{\rho_m C_{pr}}\left(u_{fl}t-x\right)}}\right]U_{step}\left(t-\frac{x}{u_{fl}}\right) \qquad ......\ (41)$$

The rock/fracture and fluid parameters for the validation purpose were given in the Table 2. The model results from the COMSOL Multiphysics were compared the work of Lauwerie's [58] and presented in Fig 4b and Fig 4c. It is clearly identified that; the error is

Journal of Energy Resources Technology. Received December 23, 2021;
Accepted manuscript posted August 28, 2022. doi:10.1115/1.4055538

less than ±5%. Thus, the proposed dynamic THM model can estimate the temperature of geofluid in the hydraulic fracture. Therefore, we can use the developed dynamic THM model to examine the het production from the geothermal reservoir.

4.2 Evolution of temperature

The spatiotemporal temperature variations in the rock matrix and fracture was examined in the present work with $SCCO_2$ and water as geofluids and presented in Fig 5 and Fig 6. The comparison between the $SCCO_2$ and water as geofluids also studied in the present work (i.e., Fig 6). From Fig 5, it has been found that temperature of the $SCCO_2$ in the fracture is gradually rising (i.e., lower to high) while moving from injection well to production well. It is due to the exchange of heat from the rock matrix to the geofluid-$SCCO_2$ and it will attain to maximum before reaching to production well. It will create a temperature difference in the fracture from injection to production well (Fig 5). It was also found that the injection/production velocity is playing an important role in the expansion of low-temperature region in the vicinity of hydraulic fracture. It has been found that the expansion of low-temperature region is fast and high in the high injection/production velocity (i.e., 0.15 m/s) scenario compared to low injection/production velocity (i.e., 0.05 m/s). Similarly, the temperature in the fracture is influenced by the injection/production velocity. The comparison of water and $SCCO_2$ as geofluids is presented in the Fig 6. At same injection/production velocity, the low temperature region is spreading comparatively faster while using water compared to $SCCO_2$.

The impact of injection velocity, initial reservoir temperature, initial reservoir temperature on the production temperature is presented in Fig 7. It has been found that, the temporal decrement in the production temperature with time and injection velocity (i.e., Fig 7a). This is because of the spreading of low temperature region in the rock matrix which is near the hydraulic fracture and it is faster in the high velocity scenario compared to low velocity. It will reduce heat extraction from the rock matrix compared to the early stages of injection-production operation, furthermore it will reduce the production temperature. Alike $SCCO_2$, production temperature was decreased temporally and increasing velocity when water is used as geofluid (Fig 7d). Initial reservoir pressure is also

Journal of Energy Resources Technology. Received December 23, 2021;
Accepted manuscript posted August 28, 2022. doi:10.1115/1.4055538

influencing the production temperature and extracting maximum production temperature at initial reservoir of 15 MPa and minimum at initial reservoir of 20 MPa (Fig 7b). It is due to the heat capacity, and thermal conductivity of $SCCO_2$ is a function of both temperature and pressure. Similar nature was not found when water using as a geofluid (Fig 7e). It is due to the properties of water are not a function of pressure and only dependent on the temperature. It was also found that, the injection temperature is influencing the production temperature. For higher injection temperature, production temperature is high compared to the low-injection temperature of the geofluid (Fig 7c). When water is used as a geofluid, injecting at low temperature (35°C) is more influencing compared to the higher temperatures (40°C and 45°C).

The comparison of both water and $SCCO_2$ as geo fluid on the production temperature was depicted in Fig 7g to Fig 7i. It was found that, steep reduction of production temperature was found when using the water compared to $SCCO_2$ with increase in injection/production velocity (Fig 7g). The initial reservoir pressure is not showing negligible impact on production temperature when using water, but it is much lesser compared to $SCCO_2$ as geofluid at constant operating conditions (Fig 7h). Similarly, injection temperature is influencing the production temperature when using water and $SCCO_2$ as geofluids, but high production temperatures were recorded when using $SCCO_2$. Fig 8 depicts the production temperature at different operating conditions when using $SCCO_2$ as geofluid. It was found that, minimum production temperature was recorded when injecting/producing $SCCO_2$ at 0.15 m/s at initial reservoir pressure of 20 MPa. Thus, $SCCO_2$ is providing the better results compared to water in the prospect of production temperature from the reservoir and also the spreading of low-temperature zone at similar operating conditions.

4.3 Evolution of stress, and strain

The variation of geomechanical properties such as stress, strain in the rock matrix and fracture are studied and presented in the present work. The Von-mises stress, Tresca stress, mechanical strain, thermal strains were examined. Von-mises stress is used to determine the fracture/yield of the rock under the load which is equal or greater than the yield strength of the rock. Fig 9 represents the spatiotemporal evolution of Von-mises

Journal of Energy Resources Technology. Received December 23, 2021;
Accepted manuscript posted August 28, 2022. doi:10.1115/1.4055538

stress (in MPa) when using $SCCO_2$ and water at injection/production velocities of 0.05 m/s and 0.1 m/s. It was found that, von-mises stress is expanding from the fracture to the rock matrix. The stress is expanding its intensity from the injection well to fracture, then to rock matrix. The distribution is regular when using $SCCO_2$ at lower injection/production velocity, and the low stress region is increasing in the vicinity of injection well (Fig $9a_1$ to $9a_5$). When using the water as geofluid, the distribution of von-mises stress is irregular after the five years of injection/production operation (Fig $9b_1$ to $9b_5$). The values in both the scenarios are less than the yield stress/elastic modulus of the rock. In both the cases the rock will not fail under the load due to the yield stress will not exceeds the yield strength of the rock. It was found that injection/production velocity is influencing the distribution of von-stress in the rock matrix along with the type of fluid. At higher the velocities (Fig 9), the distribution is irregular with time increases. At high velocities, the fluid may try to escape form the fracture to enter into the rock matrix. It will lead to restructuring of rock in the vicinity of fracture, furthermore it will create abnormalities in the rest of the rock. These abnormalities create the increase in the von-mises stress in the rock and lowering at the fracture (specifically near injection well). Thus, the type of fluid and the injection/production velocities are influencing the generation of von-mises stress (also distribution) in the rock.

The tresca stress defined as the failure of the rock occurs at a critical value of the maximum shear stress (i.e.,＝0.5yield strength of the rock). Fig 10 illustrates the tresca stress (in MPa) in the rock matrix and fracture with $SCCO_2$ and water. It was found that the distribution of tresca stress is different than the von-mises stress distributions. At the early stages the maximum tresca stress will be generates at the injection and production wells (i.e., Fig $10a_1$, $10b_1$, $10c_1$, and $10d_1$). With time progression the maximum tresca stress retain at the production well and lowest will be found in the vicinity of injection well. Specifically, minimum tresca stress will be found at the low-temperature zone compared to the rest of the reservoir. It was also found that the maximum tresca stress is found just away from the low temperature zone. The maximum value of the tresca stress is less than the maximum shear stress, thus the rock will not fail due to the shear

Journal of Energy Resources Technology. Received December 23, 2021;
Accepted manuscript posted August 28, 2022. doi:10.1115/1.4055538

stress generated during the cold fluid injection and heat extraction process. The tresca stress is dependent on the type of fluid and the injection/production velocity and it was clearly observed from the numerical results (i.e., Fig 10).

Thermal strain, mechanical strain and combined strain are computed and illustrated in Fig 11. It was found that mechanical strain is dominated compared to the thermal strain. It was observed that negative thermal strain was playing vital role in the vicinity of production and positive thermal strain was governed in the vicinity of injection well. It was also found that thermal strain is dominated in the low-temperature zone and minimum mechanical strain is found in the same zone. The thermal and mechanical strain dominated region is also dependent on the type of fluid is using. More water is entering into the rock matrix from the injection well and fracture compared to the $SCCO_2$, and it was clearly identified in the form of stress-strain variation in Fig 10 and Fig 11. It was also found that the injection/production velocity is influencing the thermal and mechanical strains. Higher the injection/production velocity, the spreading of thermal strain and mechanical strain are higher specifically in the low-temperature zone. Thus, thermal, mechanical, and combined stains are highly influenced by the type of fluid, and injection/production velocity.

4.4 Evolution of rock and fluid properties

The dynamic of fluid, rock, and fracture properties are integrated with the proposed THM model in the present work. Fig 12 depicts the variation of porosity, permeability, young's modulus, and effective thermal conductivity in the fracture and also in the matrix. It has been observed that the porosity is changed in the rock matrix, specifically in the neighborhood of fracture (Fig 12a_1 to 12a_3). This variation is due to the expansion of grain. It will decrease the pore space in the neighborhood of injection well and fracture (Fig 12a_1 to 12a_3) due to the expansion of low-temperature zone. The impact of type of injection fluid is also found in the variation of porosity. It was found that when using the water, the porosity disturbed zone is higher compared to $SCCO_2$(Fig 12b_1 to 12b_3) Similarly, the variation of porosity will be influencing the young's modulus of the rock matrix and fracture and it is presented in the Fig 12c_1 to 12c_2 when using the $SCCO_2$. The variation in the young's modulus is found very negligible compared to the initial value for both water

Journal of Energy Resources Technology. Received December 23, 2021;
Accepted manuscript posted August 28, 2022. doi:10.1115/1.4055538

and $SCCO_2$ (Fig 12c_1 to 12c_2 and Fig 12d_1 to 12d_3). It was found the permeability of rock matrix is reduced in the neighborhood of injection well with time (Fig 12e_1 to 12e_3). The reduction in permeability and porosity in the low temperature invaded zone may the cause for the pore pressure variation in the vicinity of fracture. It will be increasing with the injection/production velocities. Higher reduction of permeability zone is found while using water as geofluid (Fig 12e_1 to 12e_3 and Fig 12f_1 to 12f_3). The maximum of effective thermal conductivity (λ_{eff}) in rock matrix was found in the vicinity of fracture and decrease spatially away from the injection well (Fig 12g_1 to 12g_3 and Fig 12h_1 to 12h_3). Maximum value of λ_{eff} in fracture was observed near the injection well and it will be reduced towards the production well. These higher values are due to the low temperature near the injection well. Effective thermal conductivity will influence the heat extraction capacity from rock matrix via cold fluid injection. Thus, the physical, mechanical, and thermal properties of rock/fracture were executed efficiently and observed significant variations while injecting cold fluid.

4.5 Performance indicators of geothermal reservoir

The performance of the geothermal reservoir is studied exclusively using indicators such as thermal breakthrough time, geothermal life, reservoir impedance and the generated heat power. Thermal breakthrough is defined the time of production temperature decline was identified. In the present work we used the equation given by Rijn [58] and it is presented in eq. (42).

$$T_{\beta T} = 0.99 T_{ini} \quad \text{...... (42)}$$

In eq. (42), $T_{\beta T}$ is the thermal breakthrough, T_{ini} is the initial temperature. Thermal breakthrough time is defined as the time required for the fluid to reach thermal breakthrough at the production well. Geothermal life (ζ_l) described as the time period from the starting of the heat production to the production temperature of the reaches to 60% of the original reservoir temperature. Reservoir flow impedance is defined as the ratio of pressure difference between injection and production wells to the production flow rate [35]. Heat power represents the average extraction of heat from the geothermal reservoir while producing heat. The mathematical equations for the reservoir flow impedance and heat power are represented in eq. 43 and eq. 44, respectively [35,47,59].

$$I_{RF} = \frac{p_{inj} - p_{prod}}{q_h(t)_{prop}} \quad \text{...... (43)}$$

$$\bar{W} = \frac{W_h}{\zeta_l} = \frac{\sum_{i=1}^{\zeta_l} \left[q_h(t)_{prop} n_{prop} h_{prod} - q_h(t)_{inj} n_{inj} h_{inj} \right]_i}{\zeta_l} \quad \text{...... (44)}$$

In eq (43) and (44), p_{inj} is the injection pressure, p_{prod} is the production pressure, $q_h(t)_{prop}$ is the mass flow rate at the production well, $q_h(t)_{prop}$ is the mass flow rate at the injection well, n_{prop} is the number of production wells, n_{inj} is the number of injection wells, h_{prod} is the enthalpy at the production well, h_{inj} is the enthalpy at the injection well, ζ_l is the geothermal life. The thermal breakthrough and the geothermal life are illustrated in the Fig 7 and Fig 8. It was found the thermal breakthrough is achieved much faster when using water as geofluid. It was also found that the geothermal life is less when using water as geofluid. It was due to the intervention of water into the rock matrix from the injection well/hydraulic fracture. It will create the low-temperature zone in the vicinity of fracture and the injection well. It will reduce the heat extraction capacity of injected fluid. Thus, the production temperature decreases rapidly compared to $SCCO_2$-EGS. Similarly, $SCCO_2$-EGS system is having the better geothermal life compared to the water-EGS system.

Fig 13 depicts the impact of injection velocity, initial reservoir pressure and injection temperature on the reservoir flow impedance (RFI). It was found that the RFI is increasing with rise in injection/production velocity in both $SCCO_2$-EGS (Fig 13a) and water-EGS (Fig 13d). It was found that the RFI is independent at the higher initial reservoir pressure (i.e., 20 MPa and 25 MPa) and dependent at lower reservoir pressure (i.e., 15 MPa). Higher the injection temperature and lower the RFI in $SCCO_2$-EGS and followed ascending nature. For water-EGS system, RFI is lower when injection temperature of $35°C$ and higher when injection temperature of $40°C$ which is higher than the injection temperature of $45°C$, and $35°C$. The comparison of RFI for the water-EGS compared to the $SCCO_2$-EGS also studied found higher in water-EGS system for all three scenarios (Fig 13g, 13h, 13i). Fig 14

Journal of Energy Resources Technology. Received December 23, 2021;
Accepted manuscript posted August 28, 2022. doi:10.1115/1.4055538

depicts the RFI of the $SCCO_2$-EGS system for the injection/production velocity, initial reservoir pressure, and injection temperature. It was found that, higher RFI is found when using the injection temperature of $35°C$ and lowest was found in the case of $45°C$. But all the RFI values (both water-EGS and $SCCO_2$-EGS) are showing within the approved limit of 0.2 MPa/(kg/s) which is given by Evans [60]. Thus, the $SCCO_2$-EGS system is showing the better performance compared to the water-EGS in the prospective of RFI.

Fig 15 illustrates the impact of injection velocity, initial reservoir pressure and injection temperature on the heat power generated during the operation. It was found that these three are having significant impact on heat power for $SCCO_2$-EGS. Higher heat power was recorded for higher velocities and lower was found in low velocity (i.e., 0.05 m/s) and it was following the ascending order (Fig 15a). Lowest heat power was recorded when for a reservoir having 15 MPa initially and higher was found for 20 MPa condition (Fig 15b). It was found that when increasing injection temperature, the heat power is reducing in the $SCCO_2$-EGS which follows the descending order (Fig 15c). For water-EGS, same trend was found like $SCCO_2$-EGS with injection velocities but much higher than that of $SCCO_2$-EGS (Fig 15d and Fig 15g). It is due the density, heat capacity, and thermal conductivity of $SCCO_2$ are lower than water (Fig 2). But the injection temperature and the initial reservoir pressures are showing negligible influence on heat power for water-EGS. The comparison of RFI for the water-EGS compared to the $SCCO_2$-EGS also studied found higher in water-EGS system for all three scenarios (Fig 15g, 15h, 15i). Fig 16 depicts the heat power recorded for the $SCCO_2$-EGS system at different injection/production velocity, initial reservoir pressure, and injection temperature. It was found that, higher heat power for $SCCO_2$-EGS was recorded when using the injection temperature of $35°C$ at pressure of 20 MPa (injection velocity=0.15 m/s) and lowest was found in the case of $45°C$ and pressure of 15 MPa (i.e., injection velocity=0.05 m/s). Thus, the $SCCO_2$-EGS system is showing the lower performance compared to the water-EGS in the prospective of heat power. But showing better performance in the thermal breakthrough, geothermal life and also the RFI.

5. Conclusions

The thermo-hydro-geomechanical mathematical model was enhanced with the dynamic rock, fracture, and fluid properties in the present work. The variation of properties includes the porosity of rock/fracture, permeability of rock/fracture, young's modulus of rock/fracture, heat capacity of rock/fracture and fluid, thermal conductivity of rock/fracture and fluid, fluid viscosity, and fluid density. These variations are the functions of pressure, temperature, and stress and strains variations. This fully coupled dynamic thermo-hydro-geomechanical model was verified using the COMSOL Multiphysics 5.4 and used for the investigations of geothermal reservoir.

The present work is focused on the comparison of $SCCO_2$-EGS and water-EGS examined found the merits and demerits of the $SCCO_2$-EGS over water-EGS. Steep reduction of production temperature was identified for water-EGS system compared to $SCCO_2$-EGS system. Enhanced production temperature was recorded for the $SCCO_2$-EGS system at low inlet/outlet velocity (i.e., 0.05 m/s), and pressure of 20 MPa. The generation of Von-mises and tresca stresses the rock matrix are influenced by the injection/production velocities and type of geofluid used. Irregular distribution of von-mises stress in the rock matrix is found at higher inlet/outlet velocities. Lower tresca stress was recorded in the vicinity of fracture and maximum was found at the outer boundary of the low temperature zone. Thermal strain and mechanical strain were examined during the injection-production operation. Mechanical strain was dominated away from the low-temperature zone and thermal strain was dominated in the vicinity of hydraulic fracture. The expansion of thermal strain was highly dependent on the type of fluid (i.e., $SCCO_2$ or water) and injection/production velocity. The variation of the rock properties also presented in this work.

The performance indicator such as thermal breakthrough, geothermal life, reservoir flow impedance and heat power are determined in the present work. The $SCCO_2$-EGS system is showing better thermal breakthrough and geothermal life compared to the water-EGS system. The RFI is found within the Evans limit for the both systems and $SCCO_2$-EGS showing lowest compared to water-EGS system. The water-EGS system recorded best heat power compares to $SCCO_2$-EGS system. So, these performance indicators are highly dependent on the type of fluid, injection/production velocities, initial reservoir pressure, injection temperature. Moreover, the advantage of $SCCO_2$-EGS system over the water-EGS system gives the promising results to the geothermal industry as geofluid. It will also improve the provides the geosequestration which is not at possible in the water-EGS system.

Acknowledgement:

Manojkumar Gudala and Suresh Kumar Govindarajan gratefully acknowledge financial support from the Indian Institute of Technology–Madras; Manojkumar Gudala and Bicheng Yan thanks for the Research Funding from King Abdullah University of Science and Technology (KAUST), Saudi Arabia through the grants BAS/1/1423-01-01; Manojkumar Gudala and Shuyu Sun thanks for the Research Funding from King Abdullah University of Science and Technology (KAUST), Saudi Arabia through the grants BAS/1/1351-01-01 and URF/1/4074-01-01.

Journal of Energy Resources Technology. Received December 23, 2021;
Accepted manuscript posted August 28, 2022. doi:10.1115/1.4055538

537 **Nomenclature:**

Symbol	Description
ρ_{fl}	Density of fluid
ρ_{mat}	Density of matrix,
u_{mat}	Darcy's velocity in matrix,
u_{frc}	Darcy's velocity in fracture.
T	Temperature,
Q_{fT} and Q_{mT}	Source/sink terms fracture and matrix, respectively,
ϕ_i	Initial porosity
ϕ_{mat}	Porosity of the matrix,
C_{pfl}	Specific heat capacity of fluid,
C_{pr}	Specific heat capacity of matrix,
λ_{eff}	Effective thermal conductivity,
λ_{mat}	Thermal conductivity of matrix,
λ_{fl}	Thermal conductivity of fluid,
κ_{mat}	Rock permeability,
κ_{frc}	Permeability in fracture
κ_o	Initial permeability of the porous media
κ_{frc0}	Initial permeability of fracture
μ_{fl}	Viscosity of the fluid
a_{frc}	Fracture aperture
p_{mat}	Pressure in matrix.
p_{frc}	Pressure in fracture
ε_{vol}	Volumetric strain
M	Biot's modulus.
α_b	Biot-Wills coefficient
K_{fl}	Fluid bulk modules
K_d	Drained bulk modules
$\partial\varepsilon_v/\partial t$	Rate of change in volumetric strain of the porous matrix.
u_{di} and u_{dj}	Displacement vectors in '*i*' and '*j*' directions, respectively
∇_{Tn}	Gradient is measured on the tangential plane of fracture
q_{mat}	Source/sink term which couple both matrix and fracture $\left[-\rho_{fl}\alpha_b\left(\partial\varepsilon_{vol}/\partial t\right)\right]$
σ_s	Effective stress tensor
σ	Deviatoric stress tensor.

Journal of Energy Resources Technology. Received December 23, 2021;
Accepted manuscript posted August 28, 2022. doi:10.1115/1.4055538

$\sigma *$	Normalizing constant (and it is considered as the initial reservoir pressure)
σ_n	Normal stress.
$\Delta\varepsilon_T$	Thermal strain
α_T	Coefficient of thermal expansion
α_b	Biot-Wills coefficient
E_i	Initial elastic modulus
E_{frc}	Elastic modulus of fracture
d	Fitting parameter (constant and equal to 1)
a and *b*	Constants
C_n	Coefficient and it is a function of initial porosity of formation ($C_n = 5/\phi_i$)
k_A	Spring constant
d_A	Damping constant per unit area
u_u	Displacement in upside of fracture
u_d	Displacement in downside of fracture
u_0	Initial displacement of fracture
υ_{frc}	Poisson's ratio of fracture
d	Fitting parameter (constant and equal to 1)
U_{step}	Unit step function
u_{fl}	velocity of fluid
t	Time
x	Distance in x-direction
$erfc$	Error function
u_{di} and u_{dj}	Displacement vectors in '*i*' and '*j*' directions, respectively

References:

[1] Zhao, Y., Feng, Z., Feng, Z., Yang, D., and Liang, W., 2015, "THM (Thermo-Hydro-Mechanical) Coupled Mathematical Model of Fractured Media and Numerical Simulation of a 3D Enhanced Geothermal System at 573 K and Buried Depth 6000 e 7000 M," Energy, **82**, pp. 193–205.

[2] Sonnenthal, E. L., Smith, J. T., Cladouhos, T., Kim, J., Yang, L., Division, E. S., Berkeley, L., Ms-c, C. R., and Day, J., 2015, "Thermal-Hydrological-Mechanical-Chemical Modeling of the 2014 EGS Stimulation Experiment at Newberry Volcano

Journal of Energy Resources Technology. Received December 23, 2021;
Accepted manuscript posted August 28, 2022. doi:10.1115/1.4055538

, Oregon," **1**(2012), pp. 1–5.

[3] Vallier, B., Magnenet, V., Schmittbuhl, J., and Fond, C., 2018, "THM Modeling of Hydrothermal Circulation at Rittershoffen Geothermal Site, France," Geotherm. Energy, **6**(1), pp. 1–26.

[4] Babaei, M., and Nick, H. M., 2019, "Performance of Low-Enthalpy Geothermal Systems: Interplay of Spatially Correlated Heterogeneity and Well-Doublet Spacings," Appl. Energy, **253**, pp. 113569 (1–18).

[5] Rabemanana, V., Durst, P., Bächler, D., Vuataz, F. D., and Kohl, T., 2003, "Geochemical Modelling of the Soultz-Sous-Forêts Hot Fractured Rock Systemcomparison of Two Reservoirs at 3.8 and 5 Km Depth," Geothermics, **32**(4), pp. 645–653.

[6] Zeng, Y., Tang, L., Wu, N., and Cao, Y., 2017, "Analysis of Influencing Factors of Production Performance of Enhanced Geothermal System: A Case Study at Yangbajing Geothermal Field," Energy, **127**, pp. 218–235.

[7] Brown, D., 2000, "A Hot Dry Rock Geothermal Energy Concept Utilizing Supercritical Co2 Instead of Water," *Twenty-Fifth Workshop on Geothermal Resevoir Engineering*, pp. 1–6.

[8] Biagi, J., Agarwal, R., and Zhang, Z., 2015, "Simulation and Optimization of Enhanced Geothermal Systems Using CO2 as a Working Fluid," Energy, **86**, pp. 627–637.

[9] Zhang, F. Z., Xu, R. N., and Jiang, P. X., 2016, "Thermodynamic Analysis of Enhanced Geothermal Systems Using Impure CO2 as the Geofluid," Appl. Therm. Eng., **99**, pp. 1277–1285.

[10] Pan, C., Chávez, O., Romero, C. E., Levy, E. K., Aguilar Corona, A., and Rubio-Maya, C., 2016, "Heat Mining Assessment for Geothermal Reservoirs in Mexico Using Supercritical CO2 Injection," Energy, **102**(2016), pp. 148–160.

[11] Zhang, L., Li, X., Zhang, Y., Cui, G., Tan, C., and Ren, S., 2017, "CO2 Injection for Geothermal Development Associated with EGR and Geological Storage in Depleted High-Temperature Gas Reservoirs," Energy, **123**, pp. 139–148.

[12] Pan, L., Freifeld, B., Doughty, C., Zakem, S., Sheu, M., Cutright, B., and Terrall, T., 2015, "Fully Coupled Wellbore-Reservoir Modeling of Geothermal Heat Extraction Using CO2 as the Working Fluid," Geothermics, **53**, pp. 100–113.

[13] Olasolo, P., Juárez, M. C., Morales, M. P., Damico, S., and Liarte, I. A., 2016, "Enhanced Geothermal Systems (EGS): A Review," Renew. Sustain. Energy Rev., **56**, pp. 133–144.

[14] Liu, S., Agarwal, R., and Sun, B., 2021, "Numerical Simulation and Optimization of CO2 Enhanced Gas Recovery in Homogeneous and Vertical Heterogeneous Reservoir Models," J. Energy Resour. Technol., pp. 1–36.

[15] Pandey, S. N., Vishal, V., and Chaudhuri, A., 2018, "Geothermal Reservoir Modeling in a Coupled Thermo-Hydro-Mechanical- Chemical Approach : A Review," Earth-Science Rev., **185**(July), pp. 1157–1169.

[16] Pandey, S. N., and Chaudhuri, A., 2017, "The Effect of Heterogeneity on Heat Extraction and Transmissivity Evolution in a Carbonate Reservoir : A Thermo-Hydro-Chemical Study," Geothermics, **69**, pp. 45–54.

[17] Zhang, J., Xie, J., and Liu, X., 2019, "Numerical Evaluation of Heat Extraction for EGS with Tree-Shaped Wells," Int. J. Heat Mass Transf., **134**, pp. 296–310.

[18] Gläser, D., Flemisch, B., Helmig, R., and Class, H., 2019, "A Hybrid-Dimensional Discrete Fracture Model for Non-Isothermal Two-Phase Flow in Fractured Porous Media," GEM - Int. J. Geomathematics, **10**(1).

[19] Sun, Z., Xin, Y., Yao, J., Zhang, K., Zhuang, L., Zhu, X., Wang, T., and Jiang, C., 2018, "Numerical Investigation on the Heat Extraction Capacity of Dual Horizontalwells in Enhanced Geothermal Systems Based on the 3-D THM Model," Energies, **11**(2), pp. 1–19.

[20] Ghassemi, A., and Suresh Kumar, G., 2007, "Changes in Fracture Aperture and Fluid Pressure Due to Thermal Stress and Silica Dissolution/Precipitation Induced by Heat Extraction from Subsurface Rocks," Geothermics, **36**(2), pp. 115–140.

[21] Guo, T., Tang, S., Sun, J., Gong, F., Liu, X., Qu, Z., and Zhang, W., 2019, "A Coupled Thermal-Hydraulic-Mechanical Modeling and Evaluation of Geothermal Extraction

Journal of Energy Resources Technology. Received December 23, 2021;
Accepted manuscript posted August 28, 2022. doi:10.1115/1.4055538

in the Enhanced Geothermal System Based on Analytic Hierarchy Process and Fuzzy Comprehensive Evaluation," Appl. Energy, **258**(November 2019), p. 113981.

[22] Watanabe, N., Wang, W., McDermott, C. I., Taniguchi, T., and Kolditz, O., 2010, "Uncertainty Analysis of Thermo-Hydro-Mechanical Coupled Processes in Heterogeneous Porous Media," Comput. Mech., **45**(4), pp. 263–280.

[23] Jansen, G., Valley, B., and Miller, S. A., 2018, "THERMAID - A Matlab Package for Thermo-Hydraulic Modeling and Fracture Stability Analysis in Fractured Reservoirs."

[24] Wang, S., Huang, Z., Wu, Y. S., Winterfeld, P. H., and Zerpa, L. E., 2016, "A Semi-Analytical Correlation of Thermal-Hydraulic-Mechanical Behavior of Fractures and Its Application to Modeling Reservoir Scale Cold Water Injection Problems in Enhanced Geothermal Reservoirs," Geothermics, **64**, pp. 81–95.

[25] Lepillier, B., Daniilidis, A., Doonechaly Gholizadeh, N., Bruna, P. O., Kummerow, J., and Bruhn, D., 2019, "A Fracture Flow Permeability and Stress Dependency Simulation Applied to Multi-Reservoirs, Multi-Production Scenarios Analysis," Geotherm. Energy, **7**(1).

[26] Dobson, P. F., Kneafsey, T. J., Nakagawa, S., Sonnenthal, E. L., Voltolini, M., Smith, J. T., and Borglin, S. E., 2021, "Fracture Sustainability in Enhanced Geothermal Systems: Experimental and Modeling Constraints," J. Energy Resour. Technol. Trans. ASME, **143**(10), pp. 1–16.

[27] Zeng, Y. C., Wu, N. Y., Su, Z., Wang, X. X., and Hu, J., 2013, "Numerical Simulation of Heat Production Potential from Hot Dry Rock by Water Circulating through a Novel Single Vertical Fracture at Desert Peak Geothermal Field," Energy, **63**, pp. 268–282.

[28] Fox, D. B., Sutter, D., Beckers, K. F., Lukawski, M. Z., Koch, D. L., Anderson, B. J., and Tester, J. W., 2013, "Sustainable Heat Farming: Modeling Extraction and Recovery in Discretely Fractured Geothermal Reservoirs," Geothermics, **46**, pp. 42–54.

[29] Suzuki, A., Fomin, S. A., Chugunov, V. A., Niibori, Y., and Hashida, T., 2016,

Journal of Energy Resources Technology. Received December 23, 2021;
Accepted manuscript posted August 28, 2022. doi:10.1115/1.4055538

"Fractional Diffusion Modeling of Heat Transfer in Porous and Fractured Media," Int. J. Heat Mass Transf., **103**, pp. 611–618.

[30] Pandey, S. N., and Vishal, V., 2017, "Sensitivity Analysis of Coupled Processes and Parameters on the Performance of Enhanced Geothermal Systems," Sci. Rep., **7**(1), pp. 1–14.

[31] Dahi Taleghani, A., 2013, "An Improved Closed-Loop Heat Extraction Method From Geothermal Resources," J. Energy Resour. Technol., **135**(4), pp. 1–7.

[32] Taleghani, A. D., and Ahmadi, M., 2020, "Thermoporoelastic Analysis of Artificially Fractured Geothermal Reservoirs: A Multiphysics Problem," J. Energy Resour. Technol. Trans. ASME, **142**(8), pp. 1–13.

[33] Zhang, L., Cui, G., Zhang, Y., Ren, B., Ren, S., and Wang, X., 2016, "Influence of Pore Water on the Heat Mining Performance of Supercritical CO2 Injected for Geothermal Development," J. CO2 Util., **16**, pp. 287–300.

[34] Pan, C., Romero, C. E., Levy, E. K., Wang, X., Rubio-Maya, C., and Pan, L., 2018, "Fully Coupled Wellbore-Reservoir Simulation of Supercritical CO2 Injection from Fossil Fuel Power Plant for Heat Mining from Geothermal Reservoirs," J. CO2 Util., **27**(August), pp. 480–492.

[35] Qu, Z. qing, Zhang, W., and Guo, T. kui, 2017, "Influence of Different Fracture Morphology on Heat Mining Performance of Enhanced Geothermal Systems Based on COMSOL," Int. J. Hydrogen Energy, **42**(29), pp. 18263–18278.

[36] Yin, S., Dusseault, M. B., and Rothenburg, L., 2011, "Coupled THMC Modeling of CO 2 Injection by Finite Element Methods," J. Pet. Sci. Eng., **80**(1), pp. 53–60.

[37] Zhang, F. Z., Jiang, P. X., and Xu, R. N., 2013, "System Thermodynamic Performance Comparison of CO2-EGS and Water-EGS Systems," Appl. Therm. Eng., **61**(2), pp. 236–244.

[38] Garapati, N., Randolph, J. B., and Saar, M. O., 2015, "Brine Displacement by CO2, Energy Extraction Rates, and Lifespan of a CO2-Limited CO2-Plume Geothermal (CPG) System with a Horizontal Production Well," Geothermics, **55**, pp. 182–194.

[39] Chen, Z., Huan, G., and Ma, Y., 2006, *Computational Methods for Multiphase*

Journal of Energy Resources Technology. Received December 23, 2021;
Accepted manuscript posted August 28, 2022. doi:10.1115/1.4055538

Flows in Porous Media, Society for Industrial and Applied Mathematics.

[40] Biot, M. A., 1941, "General Theory of Three-Dimensional Consolidation," J. Appl. Phys., **12**, pp. 155–164.

[41] Biot, M. A., 1955, "Theory of Elasticity and Consolidation for a Porous Anisotropic Solid," J. Appl. Phys., **26**(2), pp. 182–185.

[42] Li, S., Feng, X. T., Zhang, D., and Tang, H., 2019, "Coupled Thermo-Hydro-Mechanical Analysis of Stimulation and Production for Fractured Geothermal Reservoirs," Appl. Energy, **247**(April), pp. 40–59.

[43] Liu, G., Pu, H., Zhao, Z., and Liu, Y., 2019, "Coupled Thermo-Hydro-Mechanical Modeling on Well Pairs in Heterogeneous Porous Geothermal Reservoirs," Energy, **171**, pp. 631–653.

[44] Freeman, T. T., Chalaturnyk, R. J., and Bogdanov, I. I., 2008, "Fully Coupled Thermo-Hydro-Mechanical Modeling by COMSOL Multiphysics , with Applications in Reservoir Geomechanical Characterization," *COMSOL Conference, Boston*, pp. 1–12.

[45] Freeman, T. T., Chalaturnyk, R. J., and Bogdanov, I. I., 2008, "THM Modeling for Reservoir Geomechanical Applications," Comsol, (October).

[46] Liu, J., 2009, "A Porosity-Based Model for Coupled Coupled Thermal-Hydraulic-Mechanical Processes."

[47] Guo, T., Tang, S., Sun, J., Gong, F., Liu, X., Qu, Z., and Zhang, W., 2020, "A Coupled Thermal-Hydraulic-Mechanical Modeling and Evaluation of Geothermal Extraction in the Enhanced Geothermal System Based on Analytic Hierarchy Process and Fuzzy Comprehensive Evaluation," Appl. Energy, **258**, p. 113981.

[48] Miller, S. A., 2015, "Modeling Enhanced Geothermal Systems and the Essential Nature of Large-Scale Changes in Permeability at the Onset of Slip," Geofluids, **15**, pp. 338–349.

[49] Touhidi-Baghini, A., 1998, "Absolute Permeability of McMurray For- Mation Oil Sands at Low Confining Stresses."

[50] Gudala, M., and Govindarajan, S. K., 2021, "Numerical Investigations on a

Geothermal Reservoir Using Fully Coupled Thermo-Hydro-Geomechanics with Integrated RSM-Machine Learning and ARIMA Models," Geothermics, **96**(May), p. 102174.

[51] COMSOL, 2018, "Subsurface Flow Module User Guide (Version 5.4)," pp. 1–256.

[52] Fokker, P. A., 2015, "Thermo-Hydro-Mechanical Modeling of EGS Using COMSOL Multiphysics," Proc. 40th Stanford Geotherm. Work., **1**, pp. 1–10.

[53] Sanaee, R., Oluyemi, G. F., Hossain, M., and Oyeneyin, M. B., 2012, "Fracture-Matrix Flow Partitioning and Cross Flow : Numerical Modeling of Laboratory Fractured Core Flood," COMSOL Conf.

[54] Norouzi, M., Dorrani, S., Shokri, H., and Anwar Bég, O., 2019, "Effects of Viscous Dissipation on Miscible Thermo-Viscous Fingering Instability in Porous Media," Int. J. Heat Mass Transf., **129**, pp. 212–223.

[55] Gudala, M., and Govindarajan, S. K., 2020, "Numerical Modelling of Coupled Single-Phase Fluid Flow and Geomechanics in a Fractured Porous Media," J. Pet. Sci. Eng., **191**, p. 107215.

[56] Gudala, M., and Govindarajan, S. K., 2020, "Numerical Modeling of Coupled Fluid Flow and Geomechanical Stresses in a Petroleum Reservoir," J. Energy Resour. Technol. Trans. ASME, **142**(6), pp. 063006(1–12).

[57] Gudala, M., and Govindarajan, S. K., 2021, "Numerical Investigations on Two-Phase Fluid Flow in a Fractured Porous Medium Fully Coupled with Geomechanics," J. Pet. Sci. Eng., **199**(December 2020), p. 108328.

[58] Rijn, S. Van, 2018, "Breakthrough Time of a Geothermal Reservoir (Estimating the Impact of Well Spacing, Reservoir and Operational Inputs on the Breakthrough Time of a Geothermal Doublet)."

[59] Zeng, Y. C., Su, Z., and Wu, N. Y., 2013, "Numerical Simulation of Heat Production Potential from Hot Dry Rock by Water Circulating through Two Horizontal Wells at Desert Peak Geothermal Field," Energy, **56**, pp. 92–107.

[60] Evans, K., 2010, "Enhanced/Engineered Geothermal System: An Introduction with Overviews of Deep Systems Built and Circulated to Date. Geothermal Energy in

Journal of Energy Resources Technology. Received December 23, 2021;
Accepted manuscript posted August 28, 2022. doi:10.1115/1.4055538

China: Past and Future," Geol. Publ. House., pp. 395–418.

Journal of Energy Resources Technology. Received December 23, 2021;
Accepted manuscript posted August 28, 2022. doi:10.1115/1.4055538

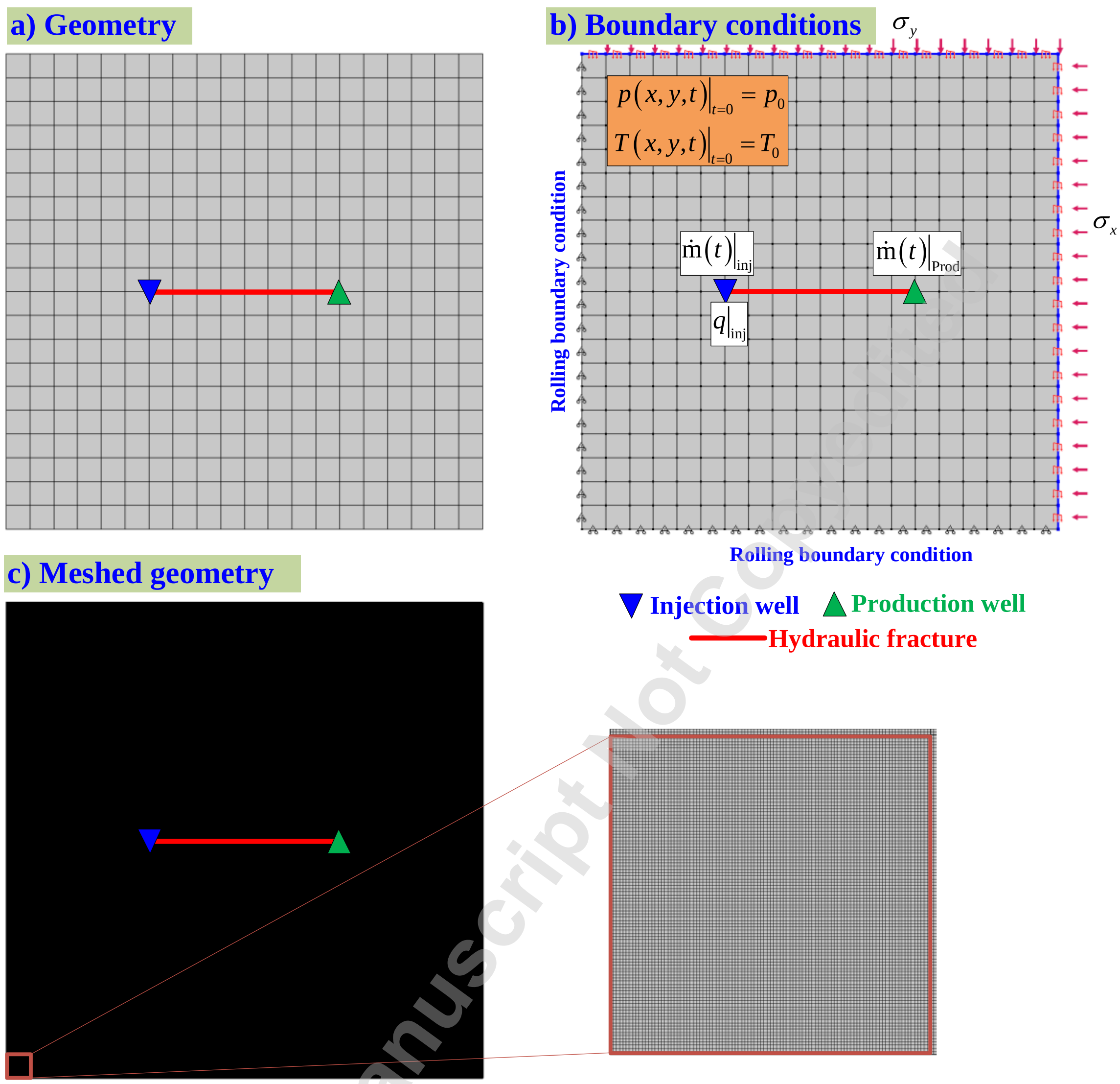

Fig 1 Geometry geothermal reservoir with single fracture (a), boundary conditions (b) and the meshed geometry (c).

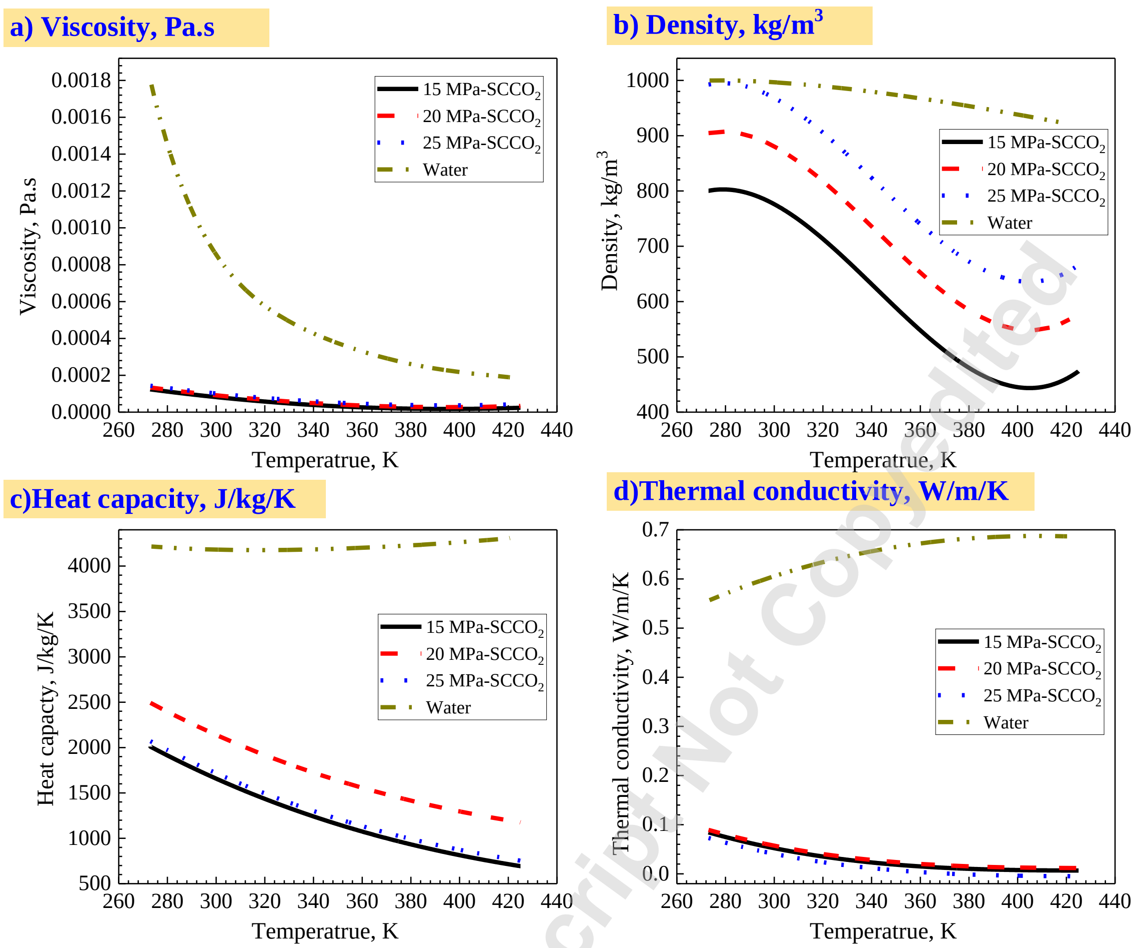

Fig 2 Comparison of the properties of $SCCO_2$ and water within the operating pressure and temperatures.

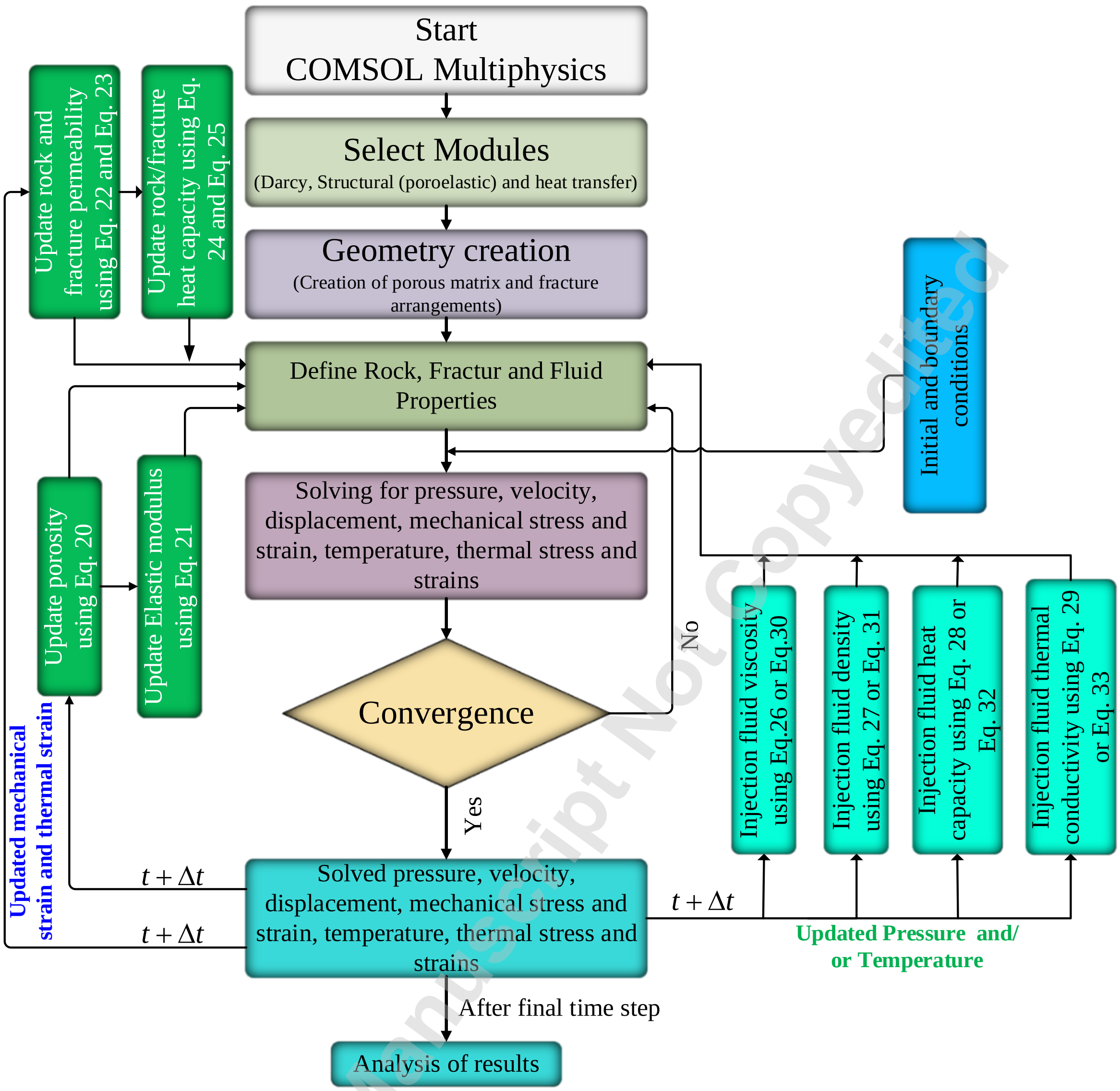

732
733 **Fig 3** Schematic of the solution process for fully coupled Thermo-hydro-geomechanical
734 model in geothermal reservoir with fracture.
735

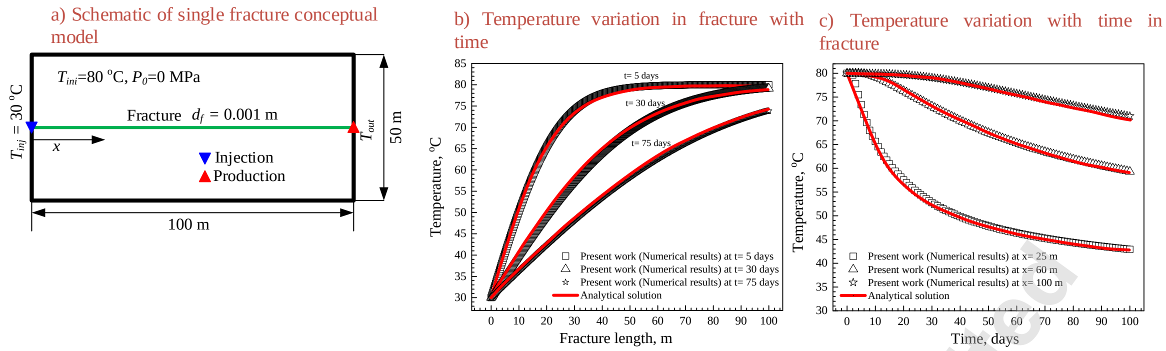

736
737 **6. Fig 4 Verification for the heat transfer in single fracture with analytical solution.**
738

Journal of Energy Resources Technology. Received December 23, 2021;
Accepted manuscript posted August 28, 2022. doi:10.1115/1.4055538

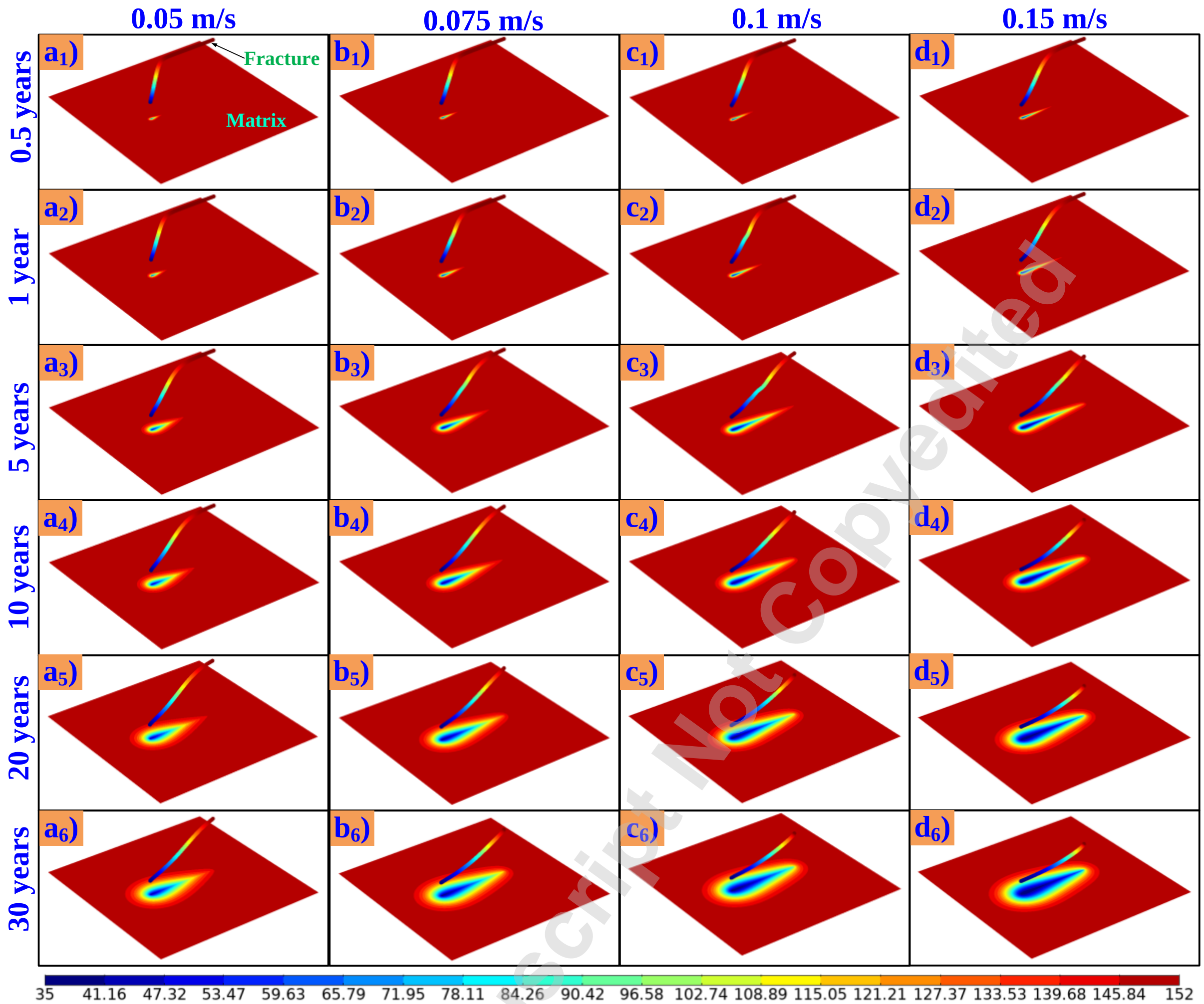

Fig 5 Spatiotemporal variation of temperature in the reservoir and fracture with different injection/production velocities when using $SCCO_2$ as geofluid at initial pressure of 15 MPa, and injection temperature of 35°C.

Journal of Energy Resources Technology. Received December 23, 2021;
Accepted manuscript posted August 28, 2022. doi:10.1115/1.4055538

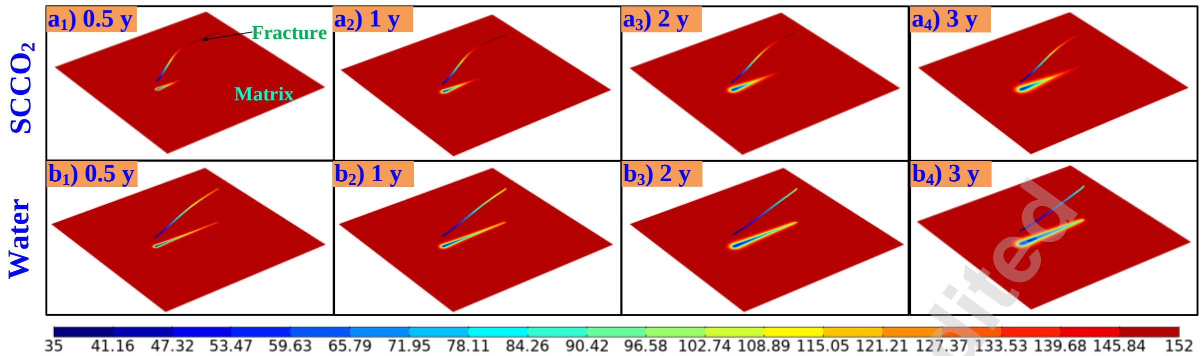

Fig 6 Comparison of $SCCO_2$ and water as geofluids on spatiotemporal variation of temperature in the reservoir and fracture at injection/production velocity of 0.1 m/s and initial pressure of 20 MPa, and injection temperature of 35°C.

Journal of Energy Resources Technology. Received December 23, 2021;
Accepted manuscript posted August 28, 2022. doi:10.1115/1.4055538

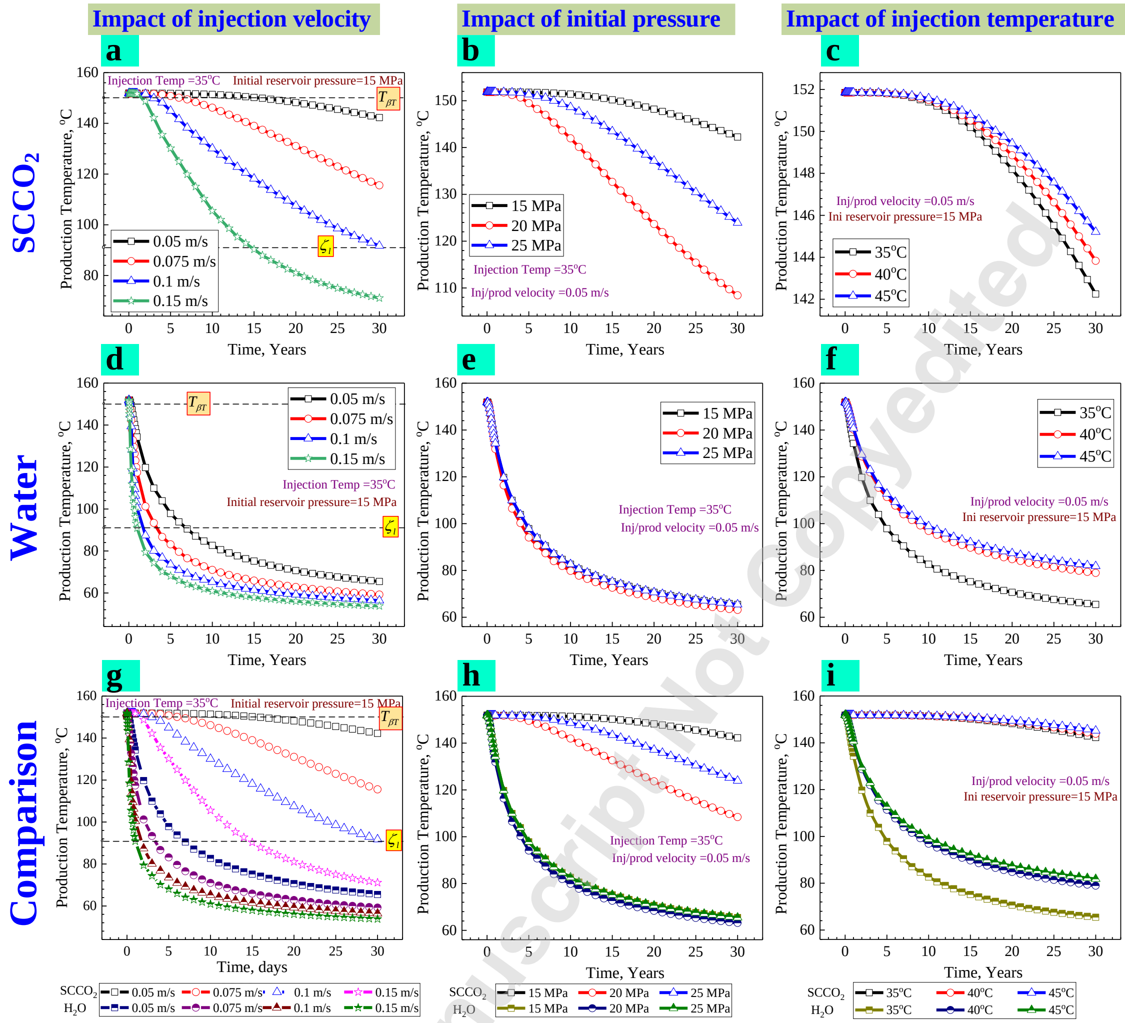

Fig 7 Impact of injection/production velocities, initial reservoir pressure, and injection temperature on the production temperature when using $SCCO_2$, and water as geofluids.

Journal of Energy Resources Technology. Received December 23, 2021;
Accepted manuscript posted August 28, 2022. doi:10.1115/1.4055538

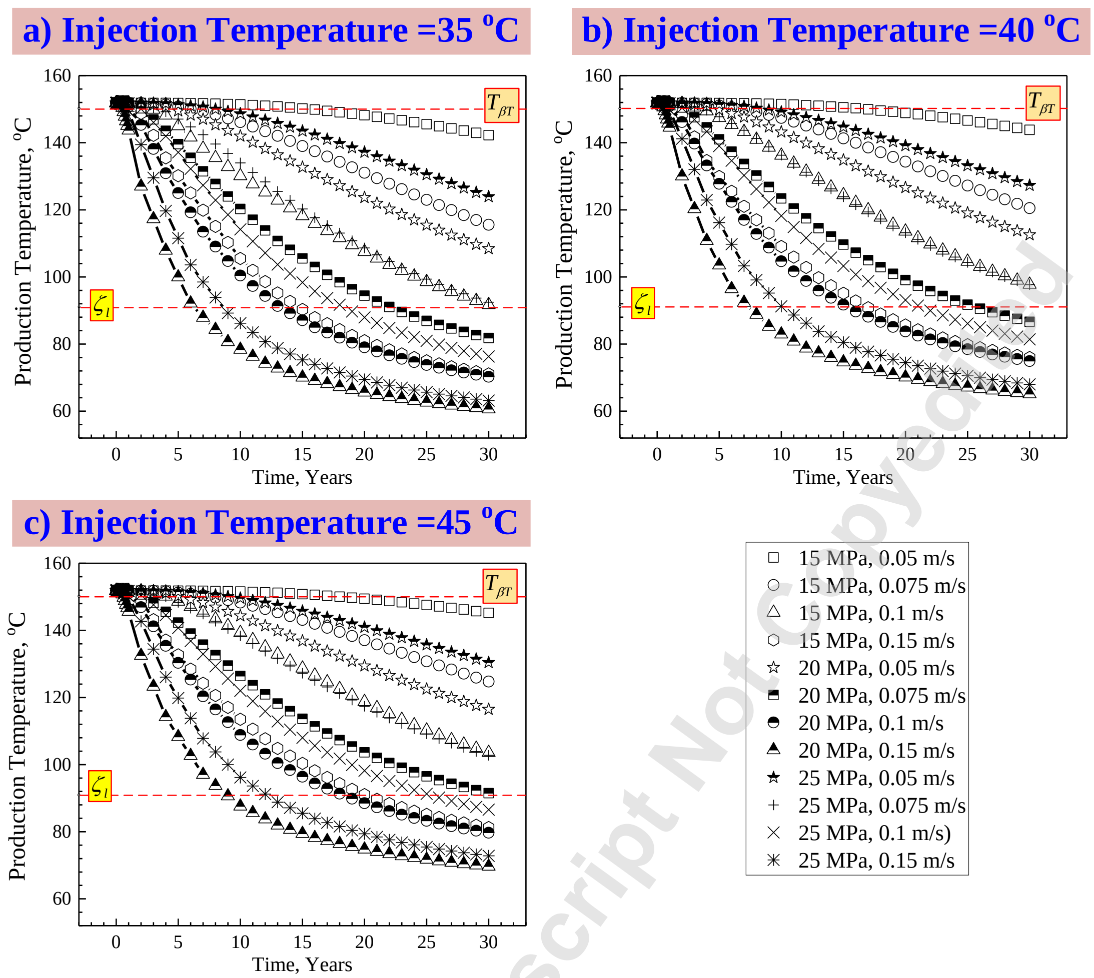

Fig 8 Production temperature when using $SCCO_2$ as geofluid at different injection rates.

Journal of Energy Resources Technology. Received December 23, 2021;
Accepted manuscript posted August 28, 2022. doi:10.1115/1.4055538

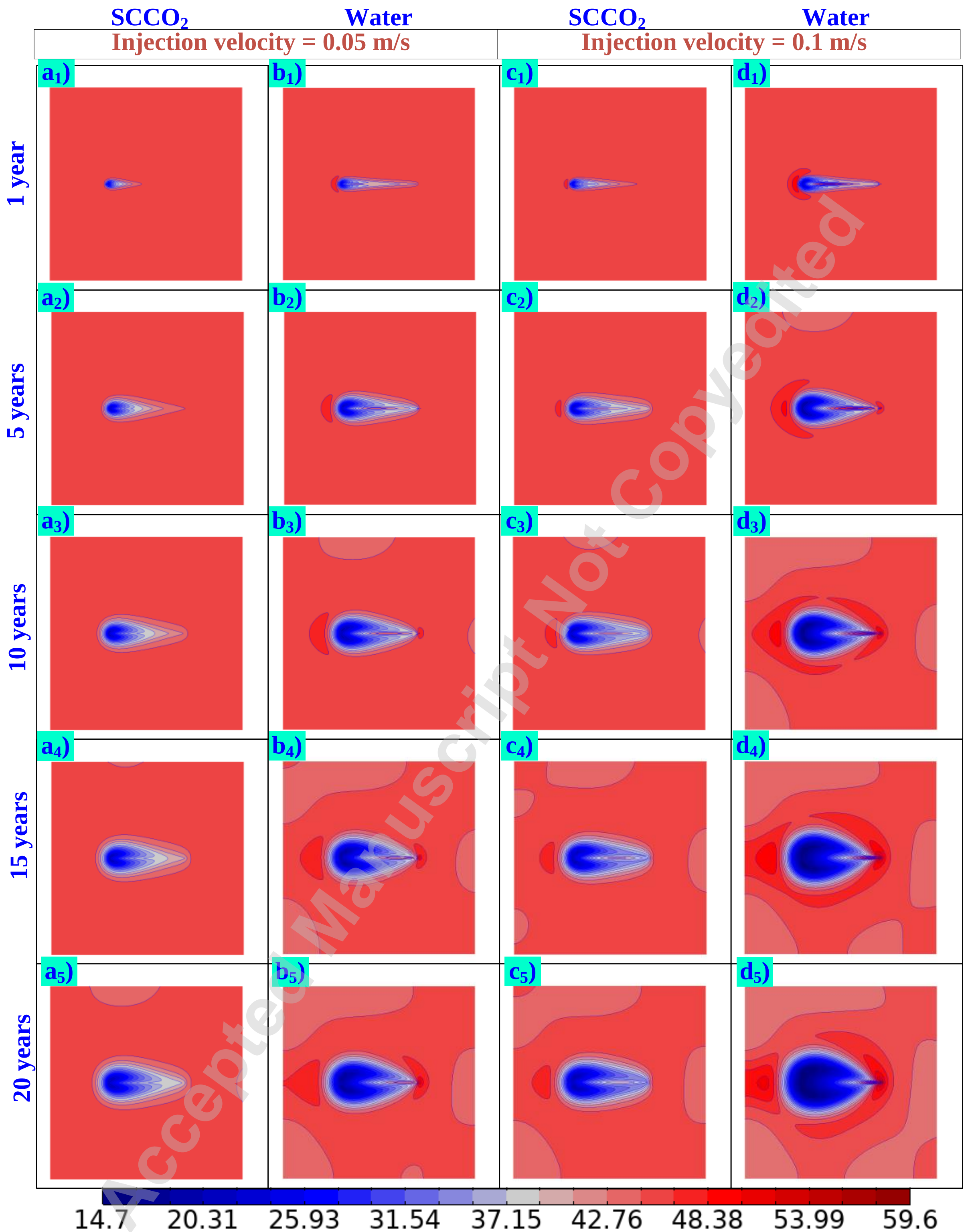

760
761 **Fig 9** Spatiotemporal variation of Von-mises stress in MPa (aperture=0.5 mm and Biot-
762 Willis's coefficient=0.5, initial reservoir pressure=20 MPa and injection
763 temperature=40°C.)
764

Journal of Energy Resources Technology. Received December 23, 2021;
Accepted manuscript posted August 28, 2022. doi:10.1115/1.4055538

765

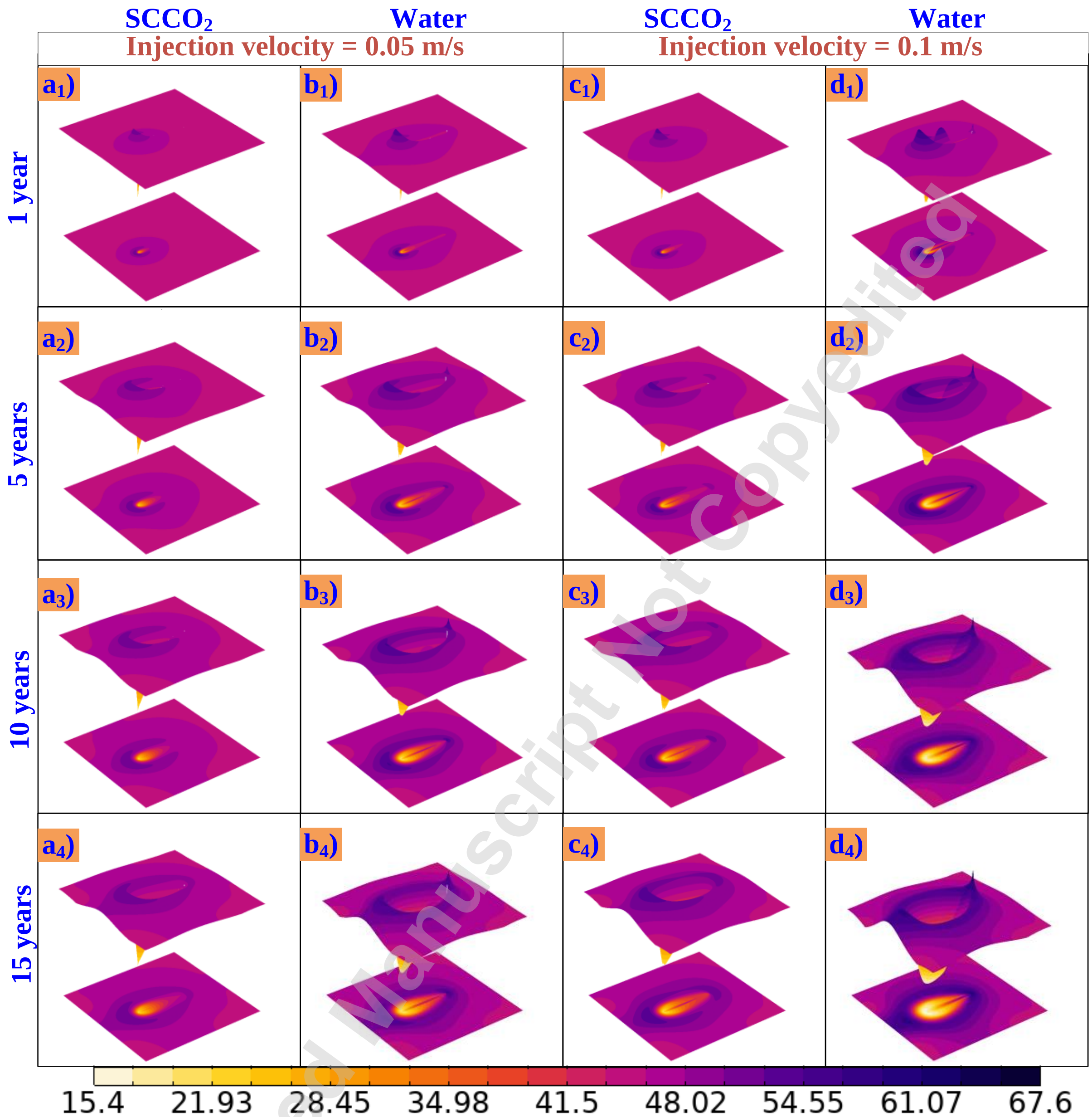

766
767 **Fig 10** Spatiotemporal variation of tresca stress in MPa (aperture=0.5 mm and Biot-Willis
768 coefficient=0.5, initial reservoir pressure=20 MPa and injection temperature=40°C.)
769
770

Journal of Energy Resources Technology. Received December 23, 2021;
Accepted manuscript posted August 28, 2022. doi:10.1115/1.4055538

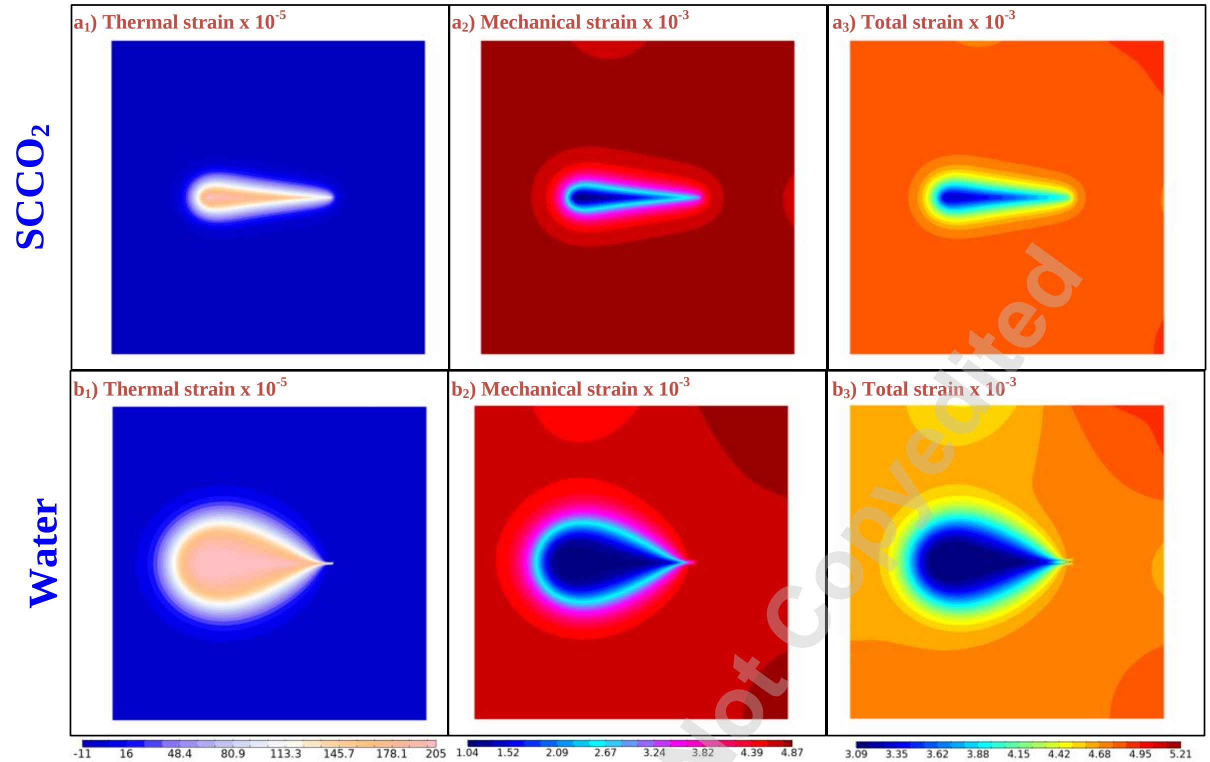

Fig 11 Spatial variation of different variants of strains after 10 years of injection and production operation (injection/production velocity= 0.05 m/s, aperture=0.5 mm and Biot-Willis coefficient=0.5, initial reservoir pressure=25 MPa and injection temperature=45°C.)

Journal of Energy Resources Technology. Received December 23, 2021;
Accepted manuscript posted August 28, 2022. doi:10.1115/1.4055538

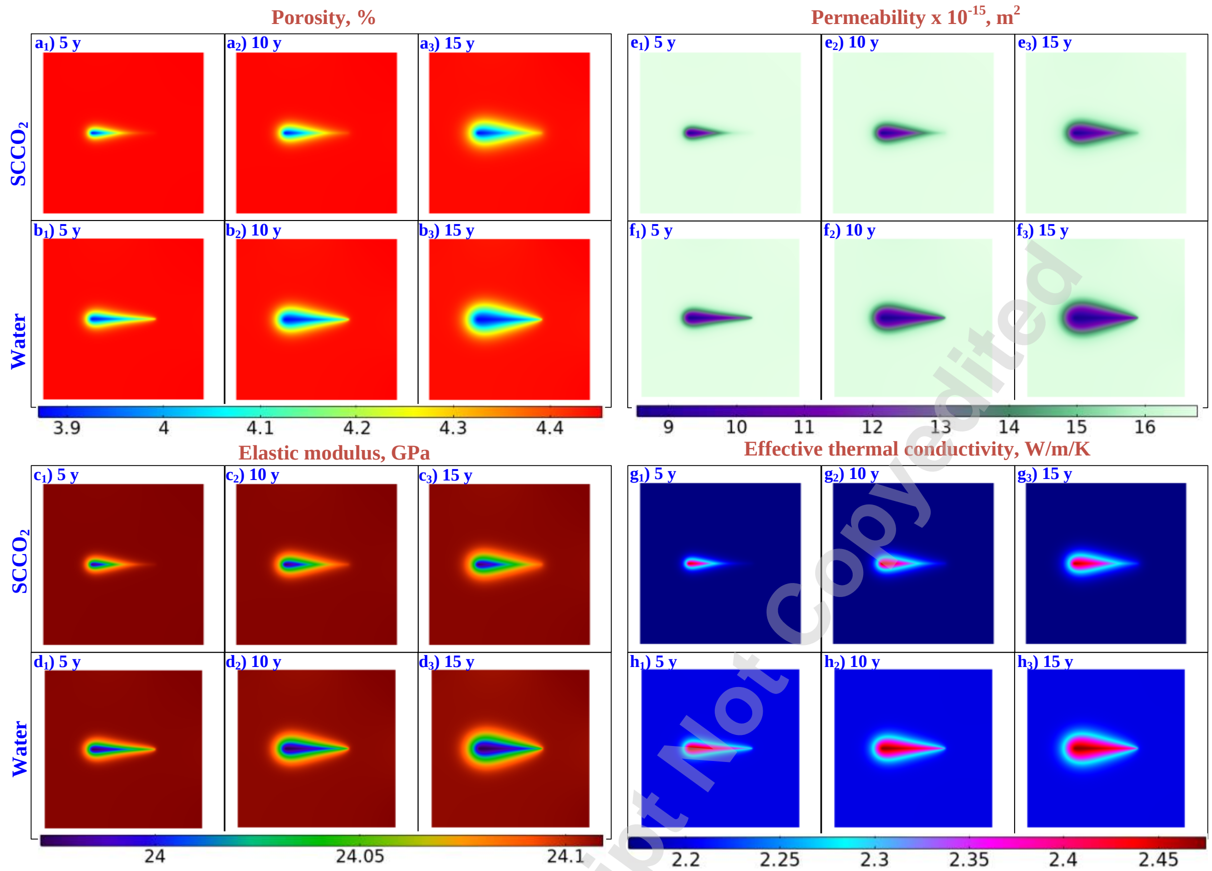

Fig 12 Spatiotemporal variation of permeability, porosity, young's modulus, and effective thermal conductivity (injection/production velocity= 0.05 m/s, aperture=0.5 mm and Biot-Willis coefficient=0. 5), initial reservoir pressure=20 MPa and injection temperature=40°C.

Journal of Energy Resources Technology. Received December 23, 2021;
Accepted manuscript posted August 28, 2022. doi:10.1115/1.4055538

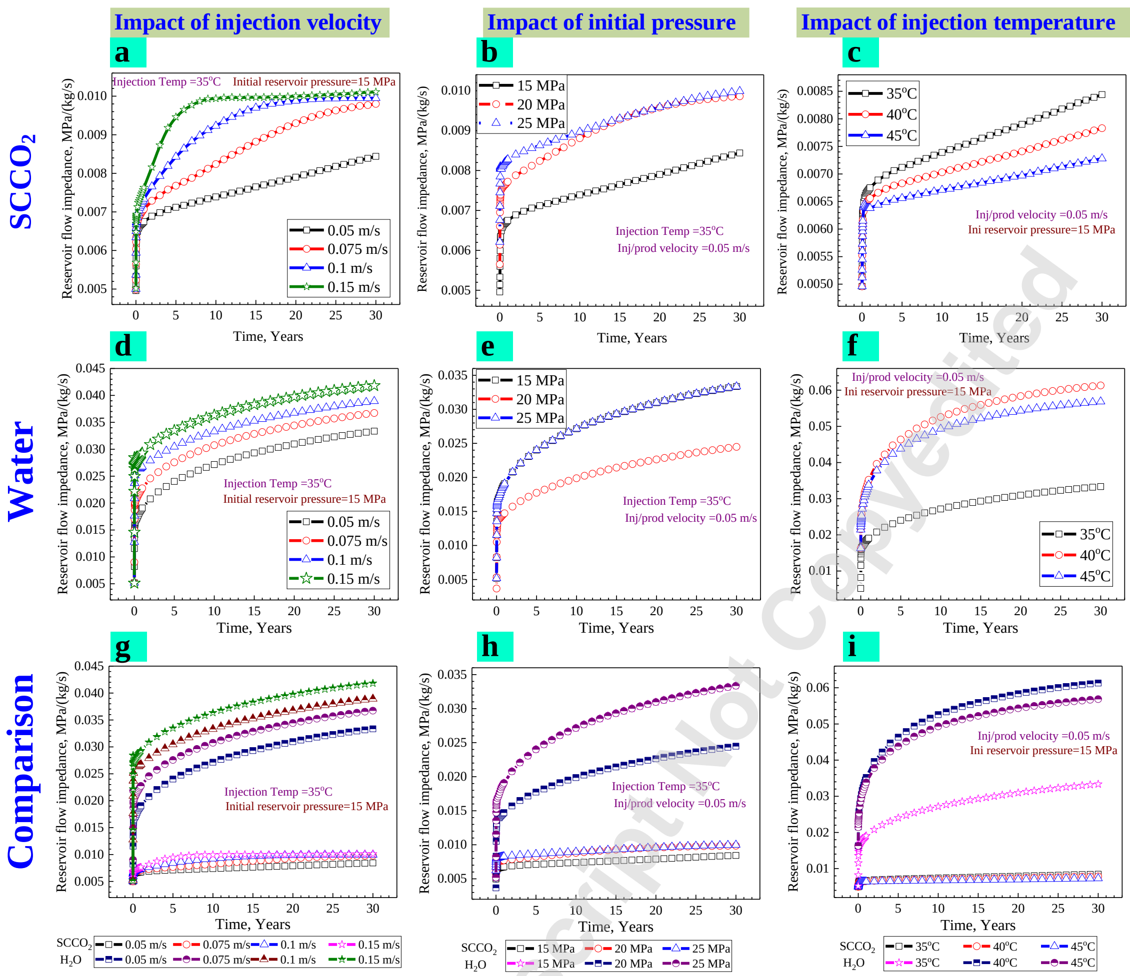

Fig 13 Impact of injection/production velocities, initial reservoir pressure, and injection temperature on the reservoir flow impedance when using $SCCO_2$, and water as geofluids.

Journal of Energy Resources Technology. Received December 23, 2021;
Accepted manuscript posted August 28, 2022. doi:10.1115/1.4055538

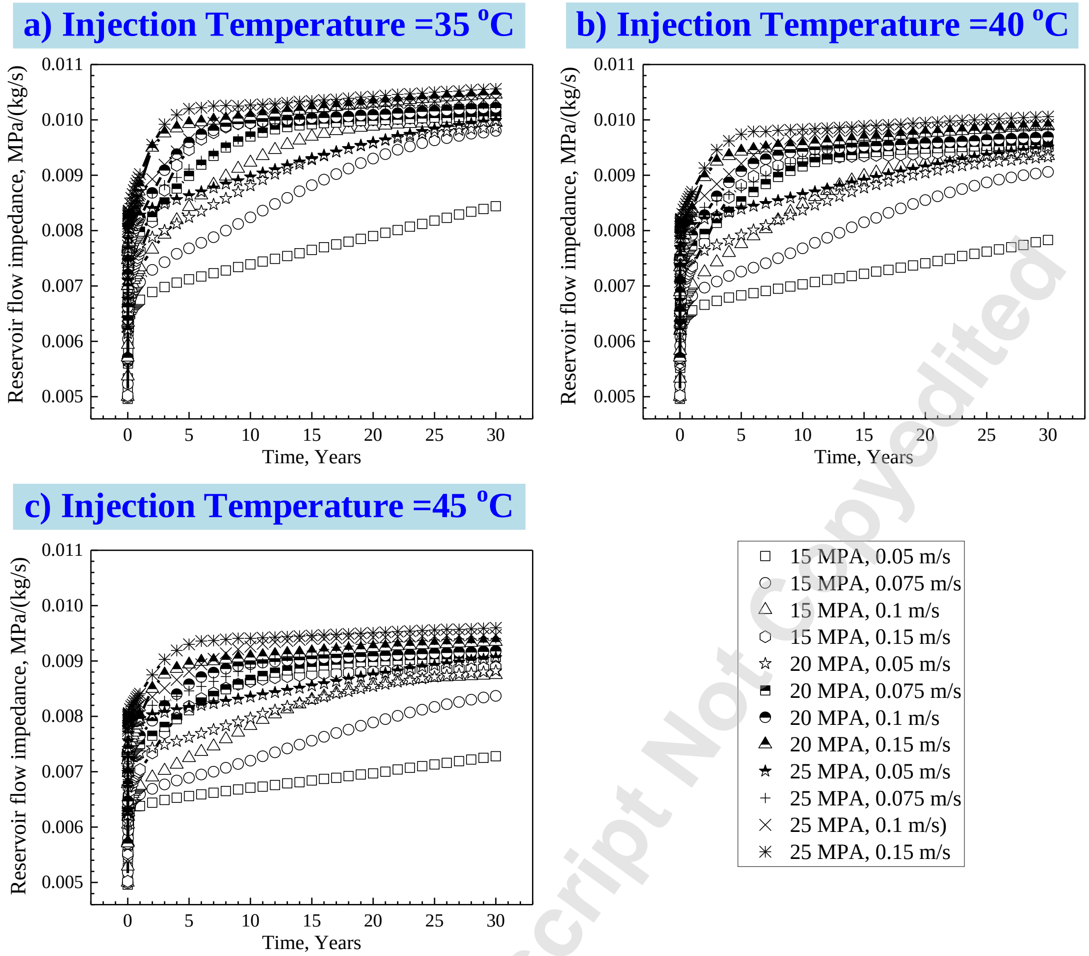

789
790 **Fig 14** Reservoir flow impedance when using $SCCO_2$ as geofluid at different injection
791 rates.

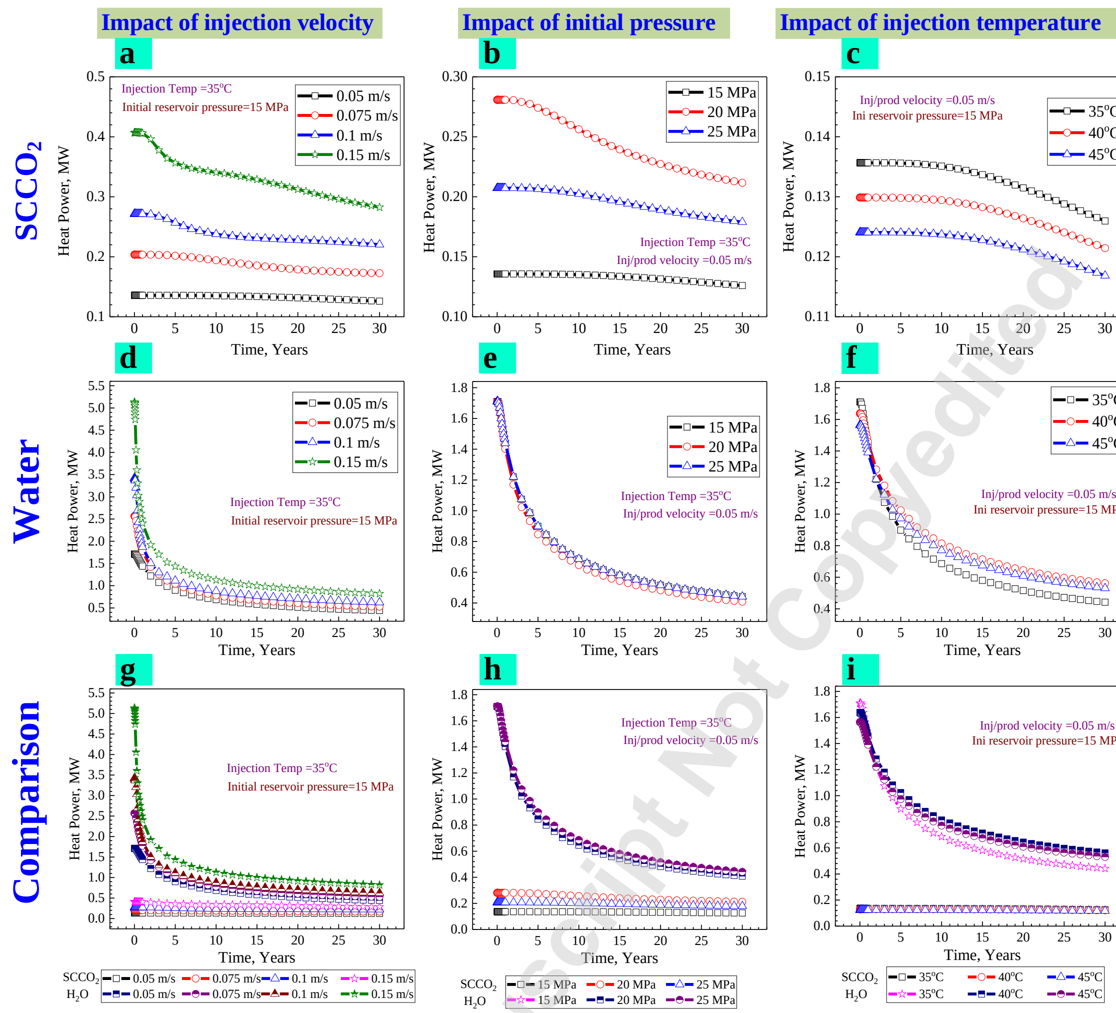

Fig 15 Impact of injection/production velocities, initial reservoir pressure, and injection temperature on the heat power when using $SCCO_2$, and water as geofluids.

Journal of Energy Resources Technology. Received December 23, 2021;
Accepted manuscript posted August 28, 2022. doi:10.1115/1.4055538

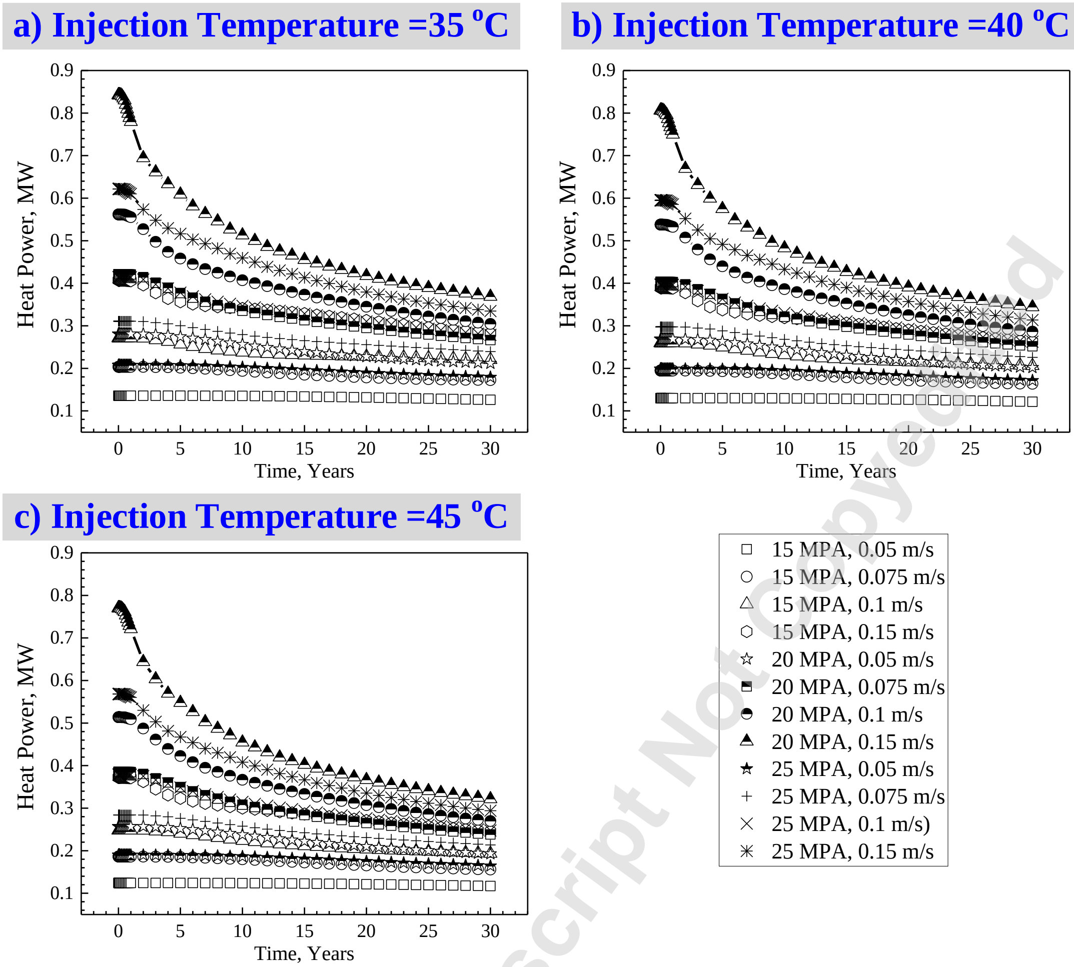

Fig 16 Reservoir flow impedance when using $SCCO_2$ as geofluid at different injection rates.

Journal of Energy Resources Technology. Received December 23, 2021;
Accepted manuscript posted August 28, 2022. doi:10.1115/1.4055538

LIST OF TABLES

Table 1 Rock matrix, fracture, and injection fluid properties

Property	Rock Properties	Fluid Properties
Density, kg/m^3	2600	Eq (27) or Eq. (31)
Dynamic viscosity, Pa.s	-	Eq (26) or Eq. (30)
Thermal conductivity, W/m.K	Eq (25)	Eq (29) or Eq. (33)
Heat capacity at constant pressure, J/kg.K	Eq (24)	Eq (28) or Eq. (32)
Coefficient of Thermal expansion, K^{-1}	2 x10^{-5}	-
Initial Youngs Modulus, GPa	24	-
Poisson's ratio	0.26	-
Initial Porosity	0.04	-
Initial Permeability, m^2	9.8692x10^{-15}	-
Ration of Specific heats	-	1.0
Biot-willis coefficient	0.5	-
Fluid-injection rate, m/s	-	0.05, 0.075, 0.1, and 0.15
Fluid-production rate, m/s	-	0.05, 0.075, 0.1, and 0.15
Initial reservoir Temperature, ℃	151.85 K	-
Fluid injection Temperature, ℃	-	35, 40, and 45
Initial Youngs Modulus-Fracture, GPa	2.4	-
Poisson's ratio-Fracture	0.104	-
Fracture aperture (d_f), mm	0.5	-
Fracture permeability, m^2	$d_f^2/12$	-
Fracture porosity	1	-
Boundary load: x-direction, MPa	48	-
Boundary load: y-direction, MPa	48	-

Journal of Energy Resources Technology. Received December 23, 2021;
Accepted manuscript posted August 28, 2022. doi:10.1115/1.4055538

Table 2 Values used for the validation of heat transfer in single fracture.

Parameter	**Numerical Value**
Rock density, kg/m³	2700
Rock Thermal conductivity, $\mathrm{W/m \cdot K}$	3.0
Rock Heat capacity at constant pressure, $\mathrm{J/kg \cdot K}$	1000
Coefficient of Thermal expansion, $\mathrm{K^{-1}}$	0.0001
Initial Youngs Modulus*, GPa	30 GPa
Poisson's ratio	0.3
Rock Initial Porosity	0.01
Initial Permeability, m²	1×10^{-7}
Ration of Specific heats	1
Biot-willis coefficient	1
Fluid density, kg/m³	1000
Dynamic viscosity, $\mathrm{Pa \cdot s}$	0.001
Fluid Heat capacity at constant pressure, $\mathrm{J/kg \cdot K}$	4200
Fluid Thermal conductivity, $\mathrm{W/m \cdot K}$	0.6
Flow velocity, m/s	0.02 m/s
Initial reservoir Temperature, °C	80
Fluid injection Temperature, °C	30

Journal of Energy Resources Technology. Received December 23, 2021;
Accepted manuscript posted August 28, 2022. doi:10.1115/1.4055538

Figure Captions List

Fig. 14	Reservoir flow impedance when using $SCCO_2$ as geofluid at different injection rates.
Fig. 15	Impact of injection/production velocities, initial reservoir pressure, and injection temperature on the heat power when using $SCCO_2$, and water as geofluids
Fig. 20	Reservoir flow impedance when using $SCCO_2$ as geofluid at different injection rates

Journal of Energy Resources Technology. Received December 23, 2021;
Accepted manuscript posted August 28, 2022. doi:10.1115/1.4055538

814 **Table Caption List**

815

Table 1	Rock matrix, fracture, and injection fluid properties
Table 2	Values used for the validation of heat transfer in single fracture

816